Asian Journal of Civil Engineering
https://doi.org/10.1007/s42107-026-01658-y

RESEARCH

Axial compressive behavior of square CFST short columns with steel plate reinforcement

Ayce Cathen Winti[1] · **Abdul Azim Abdullah**[1] · **Abdul Razak Abdul Karim**[1] · **Ahmad Beng Hong Kueh**[1,2] · **Bethany Guenevere Bronny**[1]

Received: 31 October 2025 / Accepted: 18 February 2026

Abstract

This study examines the axial compressive behavior of square concrete filled steel tube (CFST) short columns enhanced with steel plate reinforcement (SPR). Although CFST columns benefit from composite action, square sections exhibit reduced confinement effectiveness for the concrete core, increasing susceptibility to local buckling. While various strengthening methods are available, most of their implementation with prefabricated steel tubes is frequently impractical due to fabrication complexities that adversely affect construction efficiency. To overcome these issues, nine 100 mm × 100 mm × 300 mm square CFST short column specimens were tested experimentally under axial compression, including unreinforced, single SPR and double SPR configurations. SPR elements were spot welded internally to the steel tube walls to improve local stability with minimal fabrication complexity. Results confirm that SPR effectively delays local buckling onset, redistributes stress concentrations and enhances concrete confinement. Compared to unreinforced columns, specimens with SPR demonstrated increases in initial elastic stiffness (up to 63%), ductility (up to 39%) and ultimate axial compressive strength (up to 25%). Notably, double SPR configurations provided higher strength and energy absorption capacity, whereas single SPR delivered superior initial elastic stiffness and ductility, indicating a nonlinear performance relationship with reinforcement quantity. For analytical convenience, design equation is proposed to predict the axial compressive load capacity of square CFST short columns with SPR. These outcomes highlight SPR's viability as a simple, efficient strengthening alternative, offering enhanced structural performance and constructability over established methods.

Keywords Concrete filled steel tube · Steel plate reinforcement · Axial compression · Ultimate strength · Ductility

Introduction

Composite columns integrating steel and concrete serve as essential components in modern construction, leveraging the synergistic properties of both materials to form high-performance members. These elements find extensive application in skyscrapers, bridge structures and major infrastructure projects owing to their exceptional axial compressive strength, ductility and fire resistance (Abramski, 2018; Bhatia & Tiwary, 2023; George et al., 2024; Hongsong et al., 2019; Shanmugam, 2022; Sonnenschein et al., 2020; Tawfic et al., 2021). The synergistic interaction between steel and concrete significantly improves structural efficiency, positioning these composite columns as a viable substitute for conventional construction methods (Ahmed & Güneyisi, 2019; Mounica et al., 2022; Roeder et al., 2009). CFST columns represent a widely recognized form of steel-concrete composite structural systems. These structural members integrate a steel tube filled with concrete, capitalizing on the beneficial properties of both constituent materials. The steel tube provides confinement on the concrete core, increasing the concrete's compressive strength while postponing local buckling of the steel tube (Anilkumar, 2020; Megahed et al., 2024; Tan & Liu, 2012). This confinement effect improves both ductility and stiffness in CFST, rendering them particularly effective for axial load resistance and enhancing

---

✉ Ayce Cathen Winti
aycecathen@gmail.com

✉ Abdul Azim Abdullah
aaazim@unimas.my

[1] Department of Civil Engineering, Universiti Malaysia Sarawak, Kota Samarahan 94300, Sarawak, Malaysia

[2] UNIMAS Water Centre (UWC), Universiti Malaysia Sarawak, Kota Samarahan 94300, Sarawak, Malaysia

structural system stability (Diao et al., 2025; Lehman & Roeder, 2012; Ouyang & Kwan, 2018; Zhan et al., 2016).

CFST columns commonly employ circular, square or rectangular cross-sections. Circular steel tubes deliver uniform confinement to the concrete core (Le, 2023; Parvin & Brighton, 2014), as illustrated in Fig. 1(a), improving both load bearing capacity and ductility in circular CFST columns (Zhu & Chan, 2019). However, connecting I-section beams to circular columns typically requires profiled end treatments due to curved surfaces. Square steel tubes provide planar surfaces that enable direct-welded or blind-bolted connections to beam members (Chen et al., 2022; Debnath et al., 2023; Kim et al., 2015; Zhou et al., 2019), explaining their widespread practical adoption. Consequently, research on optimizing square CFST column behavior has increased in recent years. Relative to circular sections, square sections exhibit diminished confinement effectiveness throughout the cross-section (Fig. 1(a)), leaving regions near flat surfaces unconfined during steel tube local buckling. Figure 1(b) displays cracking patterns in confined square sections (Youssef et al., 2007), clearly distinguishing effective and ineffective confinement zones. Square section steel tubes with planar faces are highly susceptible to outward local buckling and necessitate stricter cross-section slenderness limits than circular sections (Huang et al., 2024; Su et al., 2020). These limitations negatively impact the square CFST column compressive performance, necessitating effective strengthening methods.

Recent experimental studies continue to emphasize that the axial compressive behavior of CFST columns is governed by the effectiveness of steel tube confinement, composite interaction between steel and concrete and the stability of steel tubes under compression. Investigations on axially loaded short columns have confirmed that local buckling of steel tubes and confinement efficiency remain dominant factors influencing axial strength, stiffness and ductility, even in CFST type systems employing refined material configurations (Lai et al., 2025; Ma et al., 2025; Nguyen et al., 2025). In parallel, recent research has highlighted the importance of steel concrete interaction and load transfer mechanisms in governing composite action and failure modes of CFST columns under axial loading, reinforcing the role of effective internal restraint in enhancing confinement performance (Deng et al., 2025; Lai et al., 2025). Although some recent approaches improve confinement through advanced material combinations or enhanced interface behavior, the fundamental challenges associated with ineffective confinement zones and premature local buckling in square CFST sections persist, particularly for thin-walled members subjected to axial compression (Lai et al., 2024).

As a result, numerous strengthening methods have been developed and investigated to address buckling phenomena in square CFST columns, aiming to optimize their structural performance under axial loading (Alatshan et al., 2020; Han et al., 2022). Existing strengthening methods for square CFST columns encompass longitudinal plate stiffeners (Guo & Diao, 2022; Tao et al., 2008, 2005), involving the welding of longitudinal plate stiffeners to the internal or external surfaces of the steel tube. Research demonstrates that such strengthening methods effectively postpone local buckling in square CFST short columns, amplifying confinement effects on the concrete core and thereby increasing both axial compressive strength and deformation resistance. Although various plate stiffener configurations were explored in previous studies (Alatshan et al., 2020), none demonstrated significant improvement in the ductility performance of square CFST columns. Another strengthening method employs binding bars installed across opposing faces of the square steel tube wall and uniformly spaced along its longitudinal axis. Experimental investigations confirmed that binding bars delay local buckling of the steel

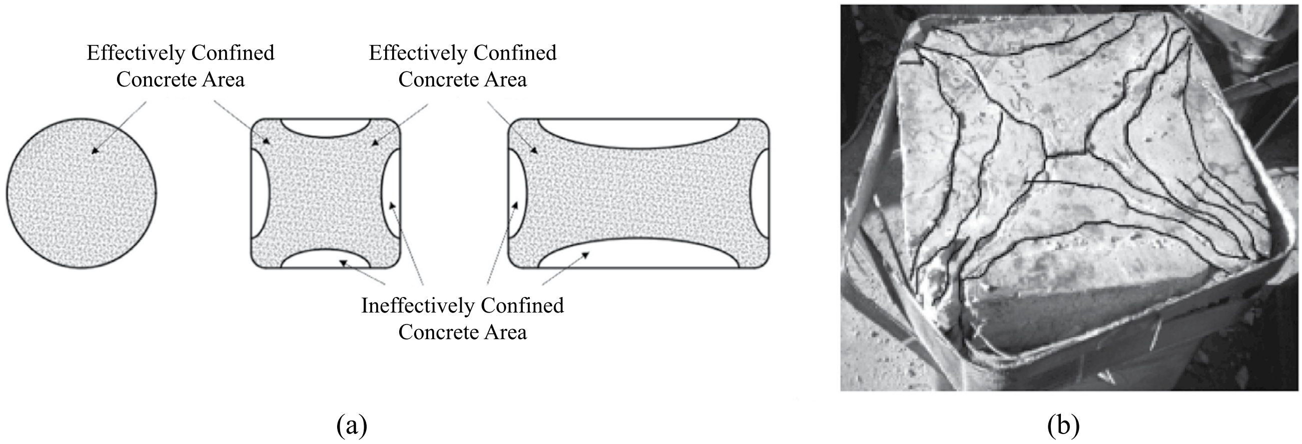

Fig. 1 Concrete confinement mechanisms: **a** Comparative confinement behavior across section geometries (Li et al., 2025; **b** Typical cracking pattern in confined square concrete section (Youssef et al., 2007)

tube and enhance lateral confinement of the concrete core (Cai & He, 2006; Cai & Long, 2007; Liao et al., 2022; Liu & Cai, 2013). However, the drilling process for bar installation was found to induce stress concentrations in the steel tube. Another strengthening method, including fiber-reinforced polymer (FRP) wraps and steel jackets, have been investigated to address these challenges. FRP wraps effectively mitigate local buckling while enhancing axial compressive strength and ductility. Steel jackets strengthen confinement and load resistance without affecting initial stiffness. However, such methods often incur higher costs and face limitations in long-term durability and constructability (Hu et al., 2011; Liao et al., 2023; Miao et al., 2023; Wen et al., 2021; Xu et al., 2025). Some of these strengthening methods are technically complex and require extensive preparation, making them difficult to implement in normal construction practices.

To address these limitations, Abdullah et al. (2018, 2020) have introduced steel plate reinforcement (SPR) in square CFST columns. The SPR elements are fixed at both ends of the internal surface of the steel tube by spot welding. This attachment method addresses the limited accessibility within small cross-sections while securing the SPR positioning during the concrete casting operation. Once the concrete cures, the interaction relies on the confinement provided by the concrete core rather than the weld strength. Their findings indicate that SPR notably improves column strength, stiffness and ductility. In those studies, the experimental results were validated through complementary finite element analysis and numerical modeling. While prior research has focused on square CFST columns with moderate slenderness, particularly under eccentric loading, a significant gap exists regarding experimental data for other section types incorporating SPR. Furthermore, no existing study has explored the influence of SPR quantity on local buckling initiation, composite interaction mechanisms and overall axial load performance.

Hence, this research experimentally examines square CFST short columns with SPR positioned inside the steel tube walls, which are then subjected to axial loading. Unlike earlier research, this investigation focuses on short columns where local buckling is the primary failure mode and SPR's effectiveness remains unknown for this type of section. The confinement action provided by SPR in square CFST short columns is also not well understood. The study also evaluates how varying SPR quantities influence structural performance. This study experimentally investigated failure modes, axial load–displacement, axial load-strain relationships, initial elastic stiffness, ductility, ultimate axial compressive strength, strength index and energy absorption characteristics of square CFST short columns. Experimental data will be utilized to assess the applicability of codified design guidelines from EN 1994-1-1, ANSI/AISC 360-22, GB 50936-2014 and AIJ. No predictive equations currently exist for estimating the axial compressive load capacity of square CFST short columns with SPR. To address this limitation, a design equation is developed to predict the axial compressive load capacity of square CFST short columns with SPR.

Experimental program

Test specimens

The experimental program comprised nine square CFST short column specimens. The experimental setup employed SPR, with all plates running continuously along the longitudinal axis and had the same height as the CFST columns. The specimens are categorized into three groups, which consist of Group CFST-X (unreinforced specimens), Group CFST-SS18 (reinforced with single SPR on each of the four sides) and Group CFST-DS18 (reinforced with double SPR on each of the four sides), as shown in Fig. 2. A 0.14B spacing ratio was chosen to maximize reinforcement capacity within the compact cross-section. This configuration allows for deeper SPR depths, compared to a lower geometric limit for equidistant spacing, while maintaining sufficient clearance to prevent aggregate blockage and ensure proper consolidation.

The SPR elements were attached via spot welding at both ends of the inner surface of the steel tubes. This attachment method was selected to address the constructability challenges associated with small cross-sections. Given the limited accessibility within the steel tubes, continuous welding along the full height was not practically feasible. Therefore, the spot welds functioned primarily as a temporary fixation to secure the SPR alignment during the concrete casting process. Once the concrete cured, the SPR was fully confined by the concrete core, ensuring effective composite action without the need for continuous welding. The spot welds were placed approximately 25 mm from each end of the steel tube, as shown in Fig. 3. The steel endplate measuring 10 mm in thickness was attached to the base of every specimen using continuous fillet welds along the entire steel tube perimeter to ensure a rigid base and prevent leakage of concrete during casting. After casting, the specimens were cured for 28 days at ambient temperature.

Table 1 presents the details and key parameters of the column specimens. All the square CFST short column

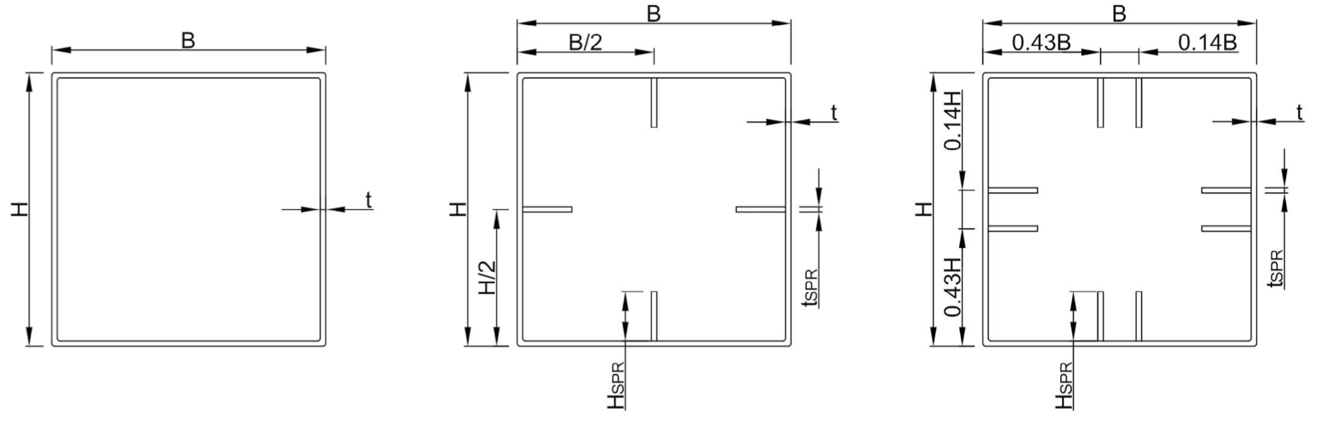

(a) (b) (c)

Fig. 2 Cross-sectional configurations of square CFST short column: **a** no SPR, **b** single SPR, **c** double SPR

Fig. 3 Typical cross-section of the specimens with longitudinal steel plate reinforcement

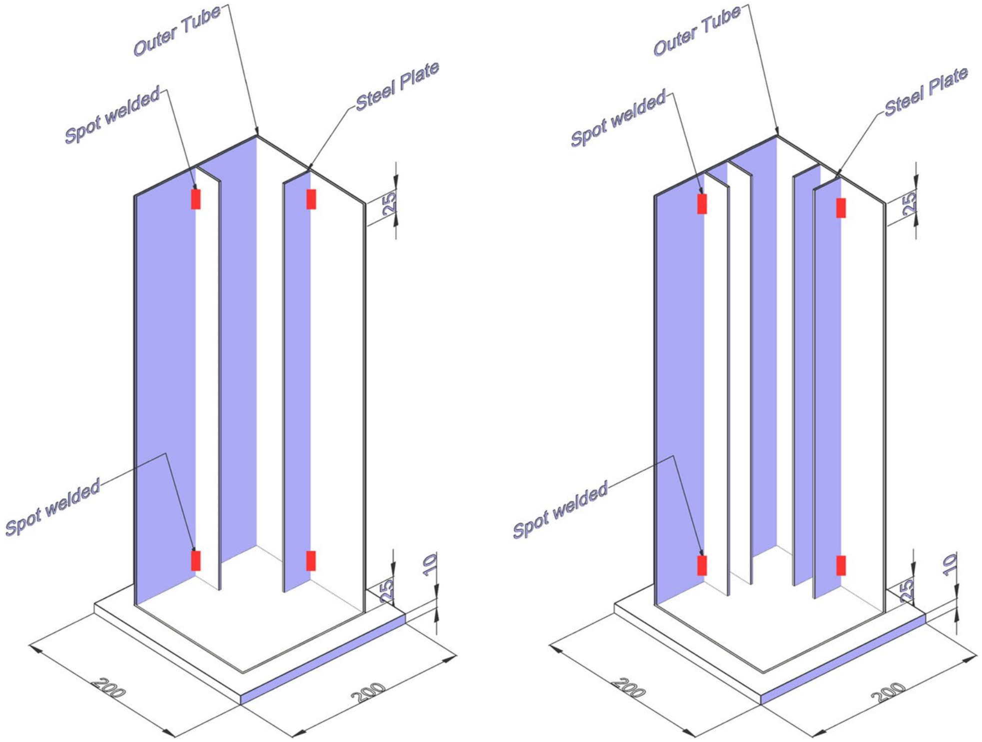

Table 1 Details of the square CFST short column specimens

Specimen	*B* (mm)	*H* (mm)	*t* (mm)	H_{SPR} (mm)	t_{SPR} (mm)	*r* (mm)	A_a (mm^2)	A_c (mm^2)	A_{SPR} (mm^2)
CFST-X-1	100.0	100.0	2.0	-	-	3.0	773.7	9212.6	-
CFST-X-2	100.0	100.0	2.0	-	-	3.0	773.7	9212.6	-
CFST-X-3	100.0	100.0	2.0	-	-	3.0	773.7	9212.6	-
CFST-SS18-1	100.0	100.0	2.0	18.0	2.0	3.0	773.7	9068.6	144.0
CFST-SS18-2	100.0	100.0	2.0	18.0	2.0	3.0	773.7	9068.6	144.0
CFST-SS18-3	100.0	100.0	2.0	18.0	2.0	3.0	773.7	9068.6	144.0
CFST-DS18-1	100.0	100.0	2.0	18.0	2.0	3.0	773.7	8924.6	288.0
CFST-DS18-2	100.0	100.0	2.0	18.0	2.0	3.0	773.7	8924.6	288.0
CFST-DS18-3	100.0	100.0	2.0	18.0	2.0	3.0	773.7	8924.6	288.0

B Steel tube sectional width, *H* Steel tube sectional depth, *t* Steel tube thickness, H_{SPR} SPR sectional depth, t_{SPR} SPR thickness, *r* Inside bend radius of steel tube, A_a Cross-sectional area of steel tube, A_c Cross-sectional area of concrete, A_{SPR} Cross-sectional area of SPR specimens have a cross-section of 100 mm × 100 mm and a height of 300 mm. This cross-sectional dimension was selected to investigate square CFST short columns governed by local buckling and steel concrete interaction, consistent with specimen sizes adopted in numerous experimental studies (Elchalakani et al., 2018; Hossain & Chu, 2019; Islam et al., 2021; Yang & Han, 2006; Yu et al., 2008). A height-to-width ratio of 3 was employed to ensure that the observed behavior was dominated by steel tube local buckling and concrete confinement rather than global instability (Alatshan et al., 2023; Ci et al., 2022; Tao et al., 2004; Wang et al., 2015; Zhou et al., 2020; Zhu et al., 2017). The selection of this scale was also governed by the 3000 kN capacity of the testing equipment, ensuring that the ultimate failure load of the reinforced specimens remained within safe operational limits. Although smaller cross-sections are known to exhibit relatively higher confinement efficiency than full-scale members, scale effects in square CFST short columns have been widely reported and acknowledged in the literature. The primary objective of this study is therefore to quantify the relative performance enhancement provided by the SPR mechanism compared to equivalent unreinforced control specimens tested under identical geometric and material conditions.

The specimen designation system identifies the experimental groups. For instance, CFST-X-1, CFST-SS18-1 and CFST-DS18-1 follow a structured naming format. The letters after the first hyphen in CFST indicate the reinforcement type, where X denotes unreinforced, SS signifies single SPR and DS represents double SPR. The number following SS or DS corresponds to the SPR sectional depth in millimetre. The final number after the second hyphen identifies the specimen within its group.

Material properties

Steel

The steel tubes and SPR employed in this experimental program were fabricated from mild steel, with both components having a thickness of 2 mm. Three standard steel coupons were machined from each steel tube and SPR using a Computer Numerical Control (CNC) system to ensure accuracy. Tensile coupon tests were conducted to determine the mechanical properties of the steels in accordance with ISO 6892-1:2019 (International Organization for Standardization, 2019), employing Hung Ta HT-2101 Electro-Hydraulic Servo Universal Testing Machines with a capacity of 300 kN. A strain gauge was mounted at the mid-height of each standard steel coupon to record the stress-strain response within the linear elastic range and to determine the Young's modulus. Beyond this, crosshead displacement was employed to capture the full plastic behavior of the standard steel coupon specimens. It is observed that the steel tube and SPR exhibit distinct stress–strain behaviors, as shown in Fig. 4. The steel tube coupons, extracted from the flat faces of the section, display a linear elastic region followed by a distinct yield plateau. This behavior is consistent with the characteristics of hot-rolled steels (Yun & Gardner, 2017), indicating that the flat faces of the steel tube retained the mechanical properties of the parent hot-rolled coil with minimal work-hardening. Conversely, the SPR material exhibits a rounded stress–strain curve with continuous yielding and no yield plateau, which is characteristic of cold-formed steels (Gardner & Yun, 2018). These results confirm that while both components are mild steel, their post-yield behaviors differ due to their specific fabrication histories. Besides, Table 2 summarizes the mean tensile properties derived from the steel tube and SPR. The

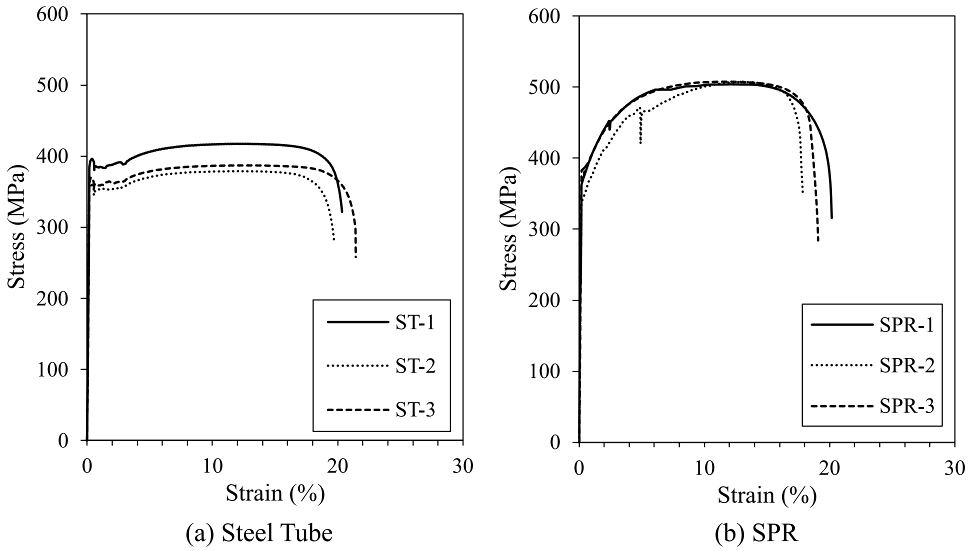

(a) Steel Tube (b) SPR

Fig. 4 Measured stress–strain curves of tensile coupons

Table 2 Mechanical properties of steel

Specimen	f_y (MPa)	f_u (MPa)	E (GPa)
Steel Tube	365.75	394.63	195.54
SPR	360.74	506.21	203.93

Table 3 Concrete mix proportion

Nominal concrete strength	Water/cement ratio	Mix proportions (to weight of cement)			
		Cement	Coarse	Fine	Water
C40	0.42	1.00	2.06	1.11	0.42

parameters include Young's modulus (E), yield strength (f_y) and ultimate tensile strength (f_u) of the tested material.

Concrete

In this study, ordinary concrete C40 was used for specimens in this test program. Table 3 details the concrete mix design. To determine the concrete compressive strength, three 150 mm concrete cubes were cast and cured under identical environmental conditions as the square CFST short column specimens. Static compression tests were performed in accordance with the MS EN 12390- 3 (Department of Standards Malaysia, 2012) to determine the unconfined compressive strength of concrete. The average cube compressive strength of concrete, f_{cu}, was 43.89 MPa.

Test setup and procedure

Axial loading was applied using a 3000 kN UTEST UTC 4730 compression machine equipped with a UTEST UTC 4850 Advanced Servo Controlled system for closed-loop loading. The axial load, end shortening, longitudinal strain and lateral strain measurements were acquired during testing. Two linear variable displacement transducers (LVDTs) were positioned symmetrically on opposite specimen sides to quantify the average axial displacement. Prior to testing, careful alignment of the specimens was carried out to achieve accurate vertical positioning, thereby minimizing potential eccentricity effects. Four strain gauges, designated SG1 to SG4, were affixed to the outer surface of the steel tube at its mid-height. Two 20 mm strain gauges (SG1 and SG3) were oriented vertically to measure longitudinal strain, while the remaining two (SG2 and SG4) were oriented horizontally to measure lateral strain. A similar approach to strain gauge installation has been adopted by previous studies (Ren et al., 2018; Sulaiman et al., 2021). Data from the LVDTs and strain gauges were continuously logged at periodic intervals using a Kyowa UCAM-60A data logger. Figure 5 presents a schematic representation of the test setup and strain gauge configuration. A monotonic load control system was employed to impose axial load directly onto the specimen surfaces at a constant rate of 5 kN/s as adopted by Chang et al. (2024), with loading continued beyond the ultimate axial compressive strength point until final failure was observed or until reaching 20 mm displacement.

Results and discussion

Failure modes

Figure 6 depicts the post-failure conditions, where all specimens ultimately failed through combined outward steel tube local buckling and concrete core crushing. While

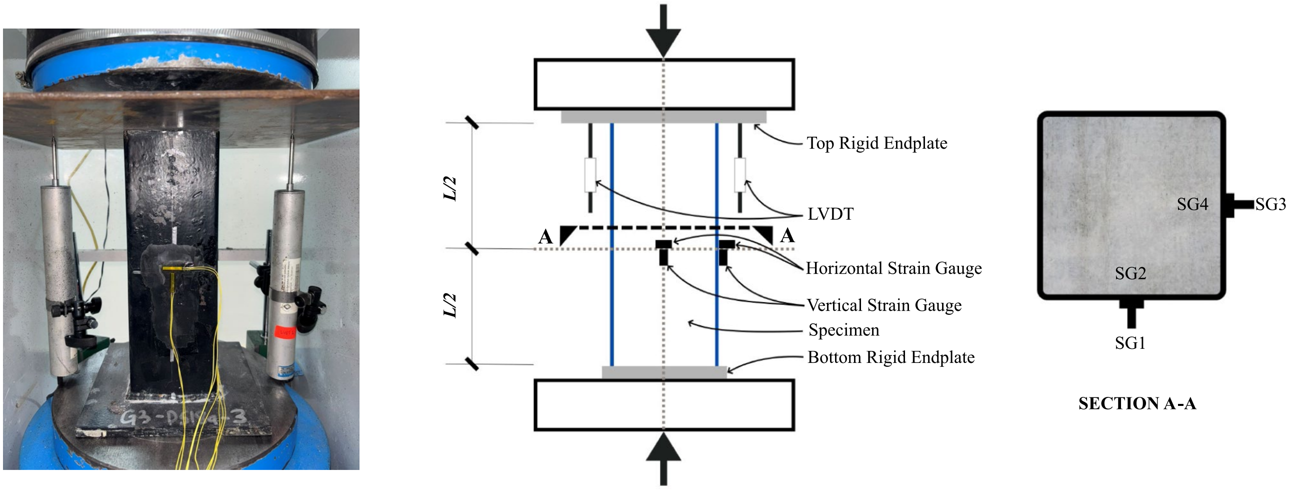

(a) (b) (c)

Fig. 5 Test setup: **a** Photograph, **b** Schematic view, **c** cross-section of the CFST

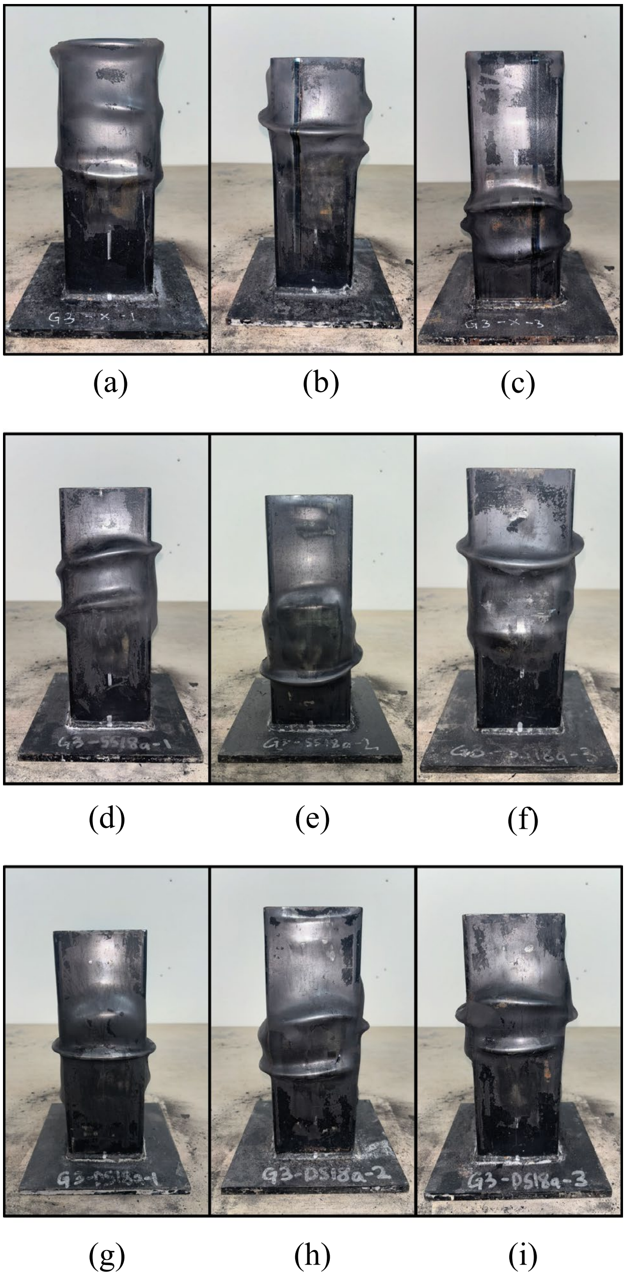

Fig. 6 Failure mode mechanisms observed in tested square CFST short column specimens: **a** CFST-X-1, **b** CFST-X-2; (**c**) CFST-X-3; (**d**) CFST-SS18-1; (**e**) CFST-SS18-2; (**f**) CFST-SS18-3; (**g**) CFST-DS18-1; (**h**) CFST-DS18-2; (**i**) CFST-DS18-3

local buckling occurred across all groups, the inclusion of SPR significantly altered the location and symmetry of the instability, indicating a shift in the failure mechanism. This behavior reflects the composite action where the steel tube limits lateral expansion and the concrete core prevents inward deformation, with maximum vertical displacement at peak load remaining below 4 mm for all specimens.

The unreinforced CFST-X specimens displayed instability concentrated near the column ends, with local buckling consistently initiating at the top region adjacent to the loading platen. This specific localization suggests that failure was driven by high stress concentrations at the platen interface, where lateral restraint is minimal. Conversely, for the reinforced groups (CFST-SS18 and CFST-DS18), the integration of SPR reinforced the steel tube walls. This effectively shifted the failure mode from premature end-instability to a more controlled local buckling at the mid-height, as illustrated in Fig. 6. Although the SPR succeeded in shifting the location of the instability, the overall failure morphology remained visually consistent across all groups. Aside from this positional shift, no other significant differences were observed in the local buckling patterns.

Post-failure inspection across all specimens further confirmed that damage was strictly localized to the concrete directly beneath these instability zones, while the adjacent intact sections sustained minimal damage, as shown in Fig. 7. Within the CFST-SS18 group, specimens CFST-SS18-1 and CFST-SS18-3 exhibited consistent structural performance. However, specimen CFST-SS18-2 deviated from this trend. As illustrated by the concrete core condition in Fig. 7(b), its inferior performance stemmed from inadequate concrete compaction, which led to premature concrete core failure and steel tube local buckling despite the presence of SPR.

Axial load–displacement response

Figure 8 illustrates the experimental axial load–displacement responses for all specimens under monotonic axial loading, highlighting the influence of SPR on structural response. The vertical axis corresponds to the axial load recorded during experimental testing, while the horizontal axis reflects the axial displacement quantified using LVDTs, with displacement values calculated as the average of measured readings. All specimens demonstrated a ductile post-peak response, characterized by a gradual descending phase, which is indicative of a controlled and progressive failure mechanism in their axial load–displacement responses. The data reveals that specimens incorporating SPR exhibit higher peak loads across the configurations, attributed primarily to the increase in cross-sectional area of the SPR. While specimens CFST-SS18-1 and CFST-SS18-3 exhibited consistent behavior with peak loads of 649.6 kN and 700.6 kN respectively, specimen CFST-SS18-2 deviated significantly from this trend. As shown in Fig. 8(b), this specimen exhibited a lower peak load (517.6 kN) and premature softening. Post-failure inspection confirmed that this discrepancy stemmed from inadequate concrete compaction, likely resulting from insufficient vibration during the casting process. This isolated fabrication defect led to

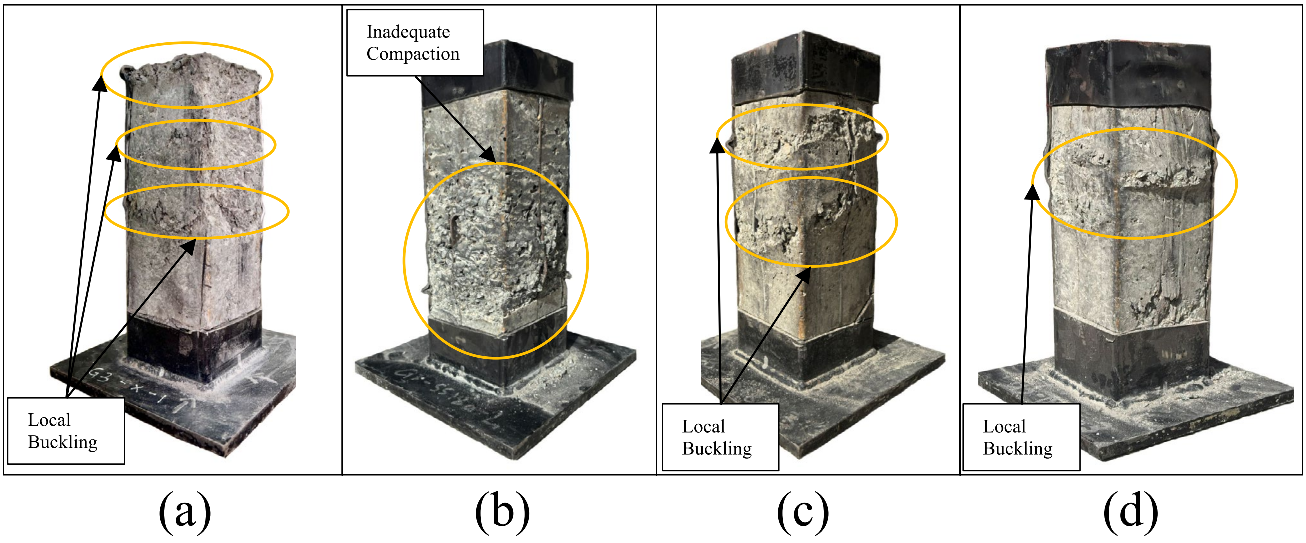

Fig. 7 Post-failure concrete core condition after removal of the steel tube for: **a** CFST-X-1; **b** CFST-SS18-2; **c** CFST-SS18-3; **d** CFST-DS18-3

premature local buckling, explaining the variation observed in Fig. 8(b).

To exemplify these mechanical properties, Fig. 9 depicts the axial load–displacement curve of the CFST-DS18-2 specimen, which highlights the structural performance of square CFST short columns with SPR under axial loading conditions. All specimens exhibit a linear rise in the elastic phase, where the applied axial load increases almost proportionally with axial displacement until yielding initiates (0.6-$-0.8N_u$). Visual inspection during Phase I (as illustrated in Fig. 9) confirmed the absence of local buckling and a minimal steel-concrete interfacial interaction across all tested specimens, indicating the specimens' linear-elastic behavior. Following the initial elastic phase, the columns transitioned to an elastic–plastic phase under increased loading, a behavior clearly captured in Phase II of Fig. 9. During this phase, the specimens exhibited early indications of local buckling, though the deformations remained subtle. In some specimens, no visible deformation was observed in this region, making it difficult to detect without close inspection. Concurrently, compressive stiffness of the specimens progressively diminished as steel components transitioned to elastic–plastic behavior, while concrete exhibited progressive crack propagation. This facilitated steel-concrete interfacial interaction, resulting in a gradual increase of the concrete core strength. Phase II concluded when structural stiffness diminished to near-zero levels (as indicated by the tangential slope of the axial load–displacement curve), marking the onset of Phase III (Fig. 9). In this final stage, specimens exhibited post-peak degradation in axial compressive strength, commencing immediately after the specimen reached its ultimate axial compressive strength. During this mechanical descending phase, all tested specimens exhibited visible local buckling deformations, alongside a pronounced steel-concrete interfacial interaction that significantly increased deformation rates. In this phase, unreinforced specimens (CFST-X) exhibit a more significant decline in strength, retaining approximately 72% of their peak load at 10 mm displacement. By comparison, single SPR specimens (CFST-SS18) sustain around 74% of their peak load, while double SPR specimens (CFST-DS18) maintain an average of 79% under the same displacement. This disparity in post-peak performance stems from the enhanced confinement provided by the SPR. By increasing the effectively confined concrete area, the SPR enables the reinforced specimens to maintain greater post-peak strength, whereas in the unreinforced specimens, local buckling compromises the lateral confining pressure on the concrete core due to the greater ineffectively confined concrete area shown in Fig. 1(a).

Axial load-strain response

Longitudinal strains (ϵ_a), which evolve in response to applied loads, provide critical insights into the yield thresholds of square CFST short columns. These axial deformations act as early indicators of structural softening, signaling the onset of material nonlinearity and potential collapse mechanisms. Conversely, lateral strains (ϵ_t) reflect the development of lateral stresses in steel components and quantify the confinement interaction between steel tubes and concrete core (Yan et al., 2019). By tracking lateral strain progression, it helps to pinpoint local buckling phenomena and assess the effectiveness of concrete confinement under incremental

Fig. 8 Axial load versus axial displacement responses of the tested specimens

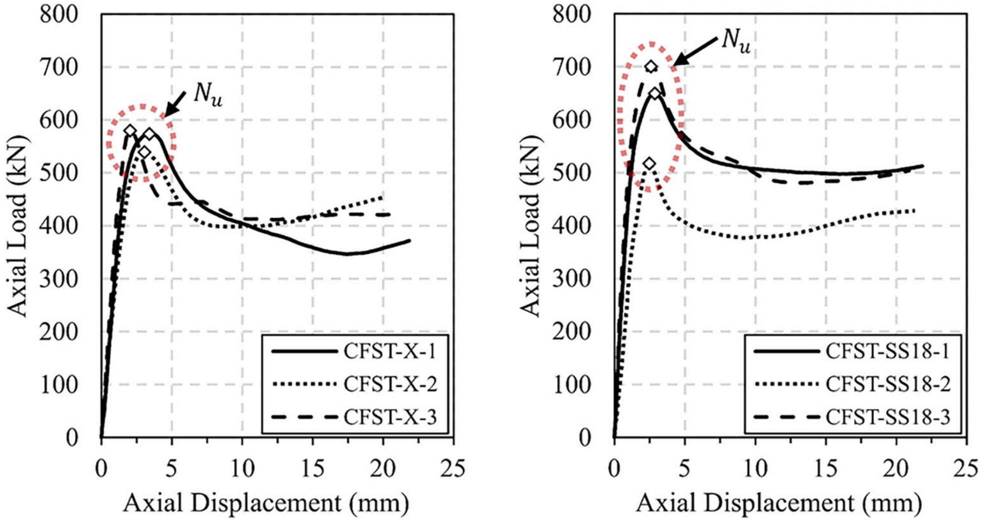

(a) CFST-X

(b) CFST-SS18

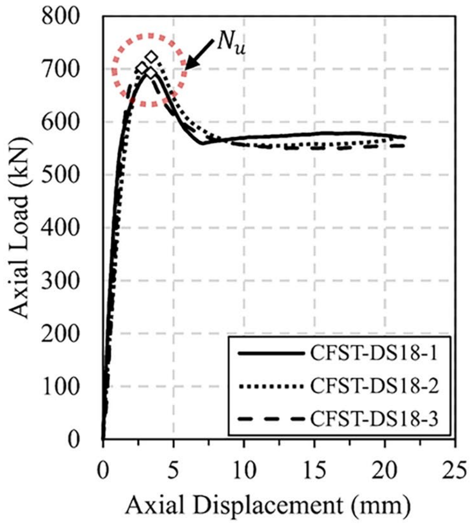

(c) CFST-DS18

loading (Du et al., 2016). Figure 10 illustrates the axial load-strain relationships for the tested specimens, characterizing their behavioral response under applied loads. It is noteworthy that the strain gauge measurements are inherently localized to their specific installation points and their readings may exhibit transient variations influenced if local buckling develops in the vicinity of the strain gauge measurement site. The longitudinal and lateral strains were measured using strain gauges installed on the steel tube surfaces at mid-height, as shown in Fig. 5. The curve adopts a sign convention wherein longitudinal strains are taken as negative values, while lateral strains are designated as positive.

Under axial load, longitudinal strain exhibits a more rapid development and greater magnitude compared to lateral strain, particularly during initial elastic phase (Phase I). As illustrated in Fig. 10, the longitudinal strain progression significantly outpaced lateral strain measurements, a trend attributed to the direct application of compressive forces along the column axis. During this phase, the axial load-strain curves exhibited a linear elastic trend, indicating the absence of local buckling in the steel tube. This behavior aligns with the proportional relationship observed in axial load–displacement curves. The transition to the elastic–plastic region (Phase II) corresponds to a marked change in material behavior. The degradation of structural stiffness observed in the load–displacement curves is explained by the longitudinal strain in the steel tube approaching its yield point. Concurrently, a discernible increase in lateral strain initiates, signifying the onset of significant lateral expansion. This expansion engages the steel tube, marking the beginning of the confinement mechanism. The effectiveness of this confinement varies significantly with the specimen

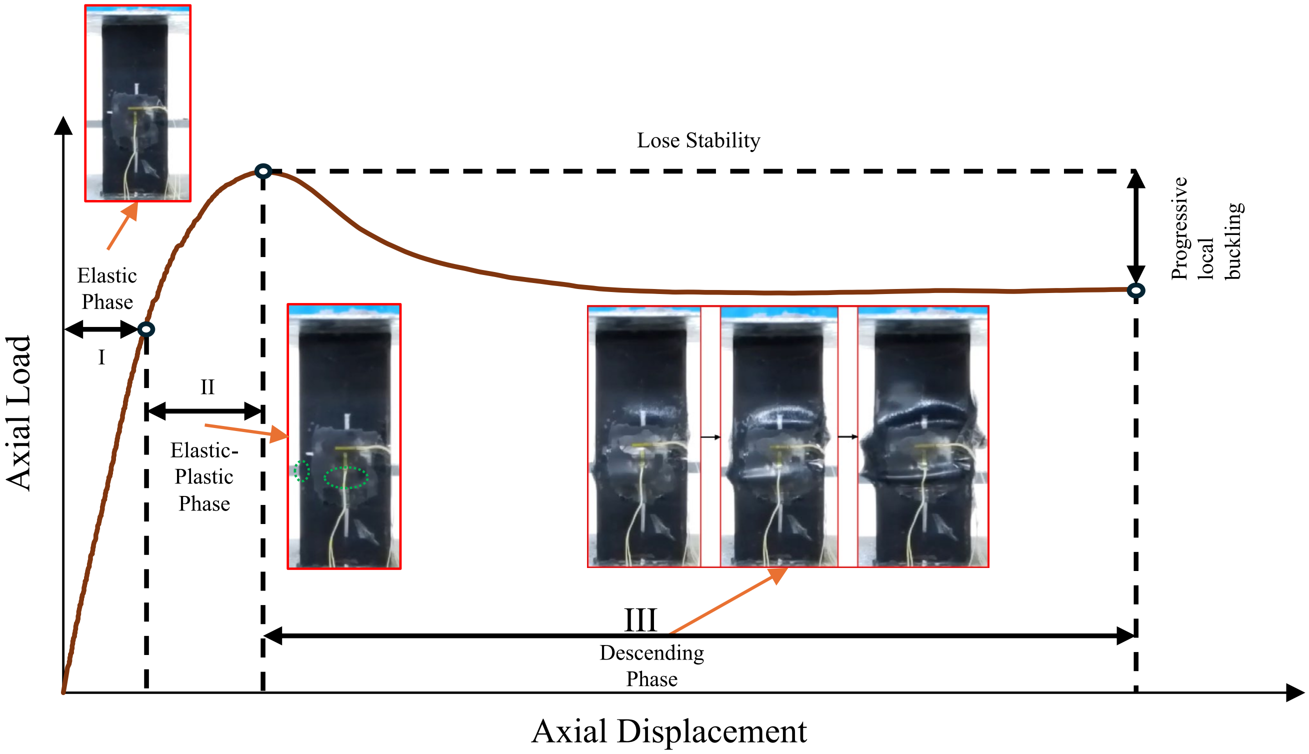

Fig. 9 Common axial load versus axial displacement response of specimen CFST-DS18-2

configuration. Unreinforced CFST-X specimens exhibit a more rapid increase in lateral strain, indicating an earlier onset of inelastic deformation and less effective restraint against concrete expansion. As the concrete core crushes in the descending branch (Phase III), it undergoes significant lateral dilation, leading to a rapid and substantial increase in lateral strain in the steel tube. This reflects the steel tube actively resisting the core's expansion, thereby providing the confinement that enables the column to maintain significant residual strength and exhibit a controlled, ductile failure.

The strain response varied significantly across specimen configurations. In general, CFST-DS18 specimens exhibited greater delayed lateral strain initiation, compared to CFST-X and CFST-SS18. This delay stems from the double SPR redistributing lateral stresses more effectively, postponing concrete expansion. In CFST-X specimens, the lack of SPR resulted in unreinforced steel tubes, triggering earlier local buckling during the elastic–plastic phase. Axial load-strain curves for unreinforced specimens displayed abrupt post-peak degradation, attributed to inadequate lateral confinement and early local buckling of the steel tube, which compromised stress transfer to the concrete core. In contrast, the sustained and stable progression of lateral strain in the SPR-strengthened specimens, particularly CFST-DS18, confirms an enhanced confinement effect that improves both the deformation capacity and overall ductility of the composite column.

Effectiveness of steel plate reinforcement

To assess the influence of SPR on the structural performance of square CFST short column specimens, critical parameters such as initial elastic stiffness, ductility, ultimate axial compressive strength, strength index and energy absorption capacity were measured and determined. A detailed summary of the experimental findings is provided in Table 4.

Initial elastic stiffness

Steel demonstrates a nearly linear stress–strain relationship prior to reaching its elastic limit. In contrast, the formation of microcracks in concrete results in a decline in the secant modulus with rising stress levels (Neville, 1995). The modulus of elasticity for concrete (E_c) is commonly characterized in practical applications as the secant value approximated between $\sigma = 0$ and $0.4f_c$, where f_c denotes the compressive strength of the concrete, according to MS EN 1992-1-1:2010 (Department of Standards Malaysia, 2010). In CFST columns, the secant compressive stiffness diminishes under higher compressive loads due to concrete cracking. Studies by Huo et al. (2009) and Yang et al. (2013) define compressive stiffness as the secant value at 40% of the ultimate axial

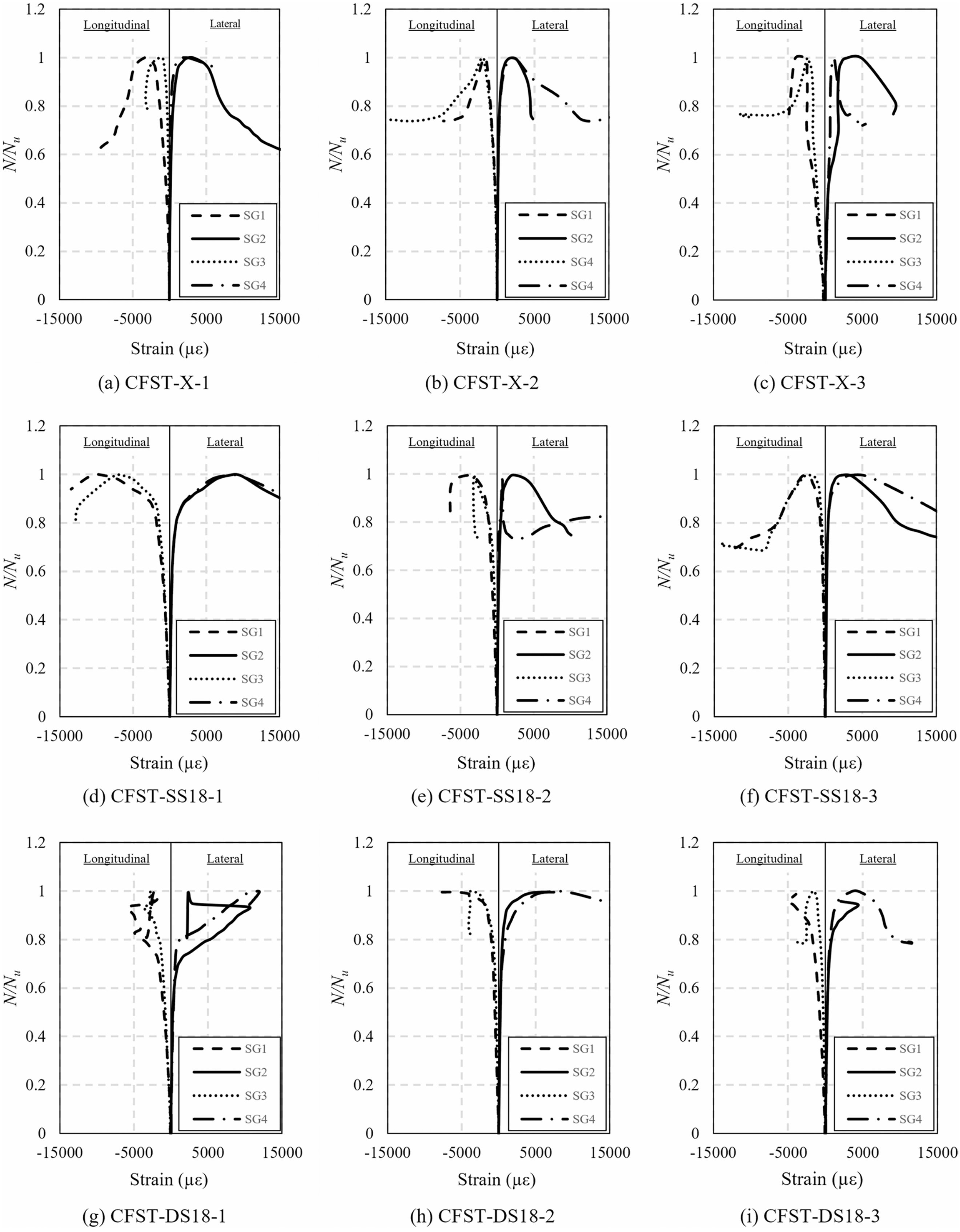

(a) CFST-X-1 (b) CFST-X-2 (c) CFST-X-3

(d) CFST-SS18-1 (e) CFST-SS18-2 (f) CFST-SS18-3

(g) CFST-DS18-1 (h) CFST-DS18-2 (i) CFST-DS18-3

Fig. 10 Axial load versus strain responses of the tested specimens

Table 4 Summary of experimental test results

Specimen	θ	Ductility		Ultimate axial strength			Energy absorption capacity		
		DI	*DEI*	N_u (kN)	*SI*	*UEI*	EA_{pre} (J)	EA_{post} (J)	EA_t (J)
CFST-X-1	0.84	2.92	1.00	574.0	0.928	1.00	1369.5	6767.2	8136.7
CFST-X-2	0.84	2.67		539.2	0.872		1102.8	7266.4	8369.3
CFST-X-3	0.84	2.21		580.4	0.939		730.6	7832.3	8562.9
CFST-SS18-1	1.01	3.64	1.39	649.6	0.977	1.20	1343.6	8974.9	10318.5
CFST-SS18-2	1.01	-[1]		517.6	-[1]		-[1]	-[1]	-[1]
CFST-SS18-3	1.01	3.58		700.6	1.053		1298.1	9106.8	10404.9
CFST-DS18-1	1.19	4.15	1.37	691.8	0.972	1.25	1781.1	9792.1	11573.2
CFST-DS18-2	1.19	2.99		722.1	1.015		1702.0	9691.1	11393.1
CFST-DS18-3	1.19	3.56		701.7	0.986		1311.7	9882.2	11193.9

θ Confinement Ratio, *DI* Ductility Index, *DEI* Ductility Enhancement Index, N_u Ultimate Axial Compressive Strength, *SI* Strength Index, *UEI* Ultimate Axial Compressive Strength Enhancement Index, EA_{pre} Pre-peak Energy Absorption, EA_{post} Post-peak Energy Absorption, EA_t Total Energy Absorption

[1] Result is not included because of poor concrete compaction

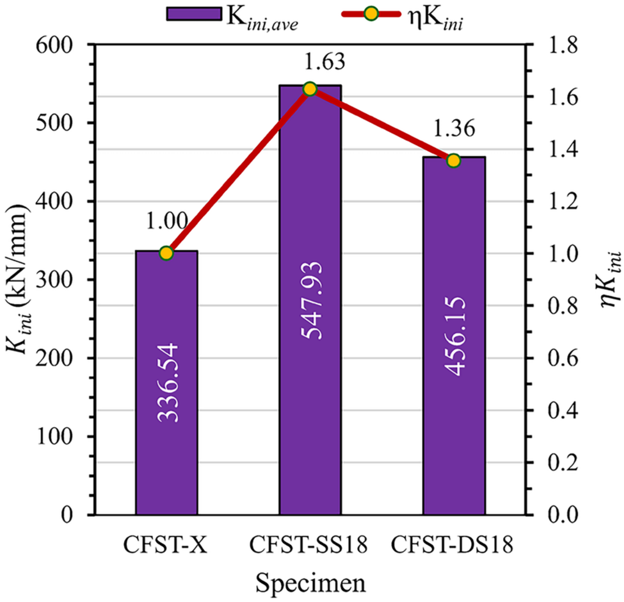

Fig. 11 Effect of SPR on the initial elastic stiffness of specimens

strength. Accordingly, the initial elastic stiffness (K_{ini}) of the square CFST short column is defined by the following equation, as adopted by Ayough et al. (2022).

$$K_{ini} = \frac{0.4N_u}{\Delta_{0.4}} \tag{1}$$

where N_u represents the ultimate axial compressive strength and $\Delta_{0.4}$ represents the axial displacement at $0.4N_u$ during the pre-peak stage of the curve.

The enhancement of initial elastic stiffness was quantified using the stiffness enhancement index ($\eta_{K_{ini}}$). This index was computed via the following equation:

$$\eta_{K_{ini}} = \frac{K_{ini,SPR}}{K_{ini,0}} \tag{2}$$

where $K_{ini,SPR}$ and $K_{ini,0}$ denote the initial elastic stiffness of square CFST short columns incorporating SPR and their unreinforced counterparts, respectively.

The incorporation of SPR consistently enhanced average initial elastic stiffness ($K_{ini,ave}$), with the single SPR specimen (CFST-SS18) and double SPR specimen (CFST-DS18) exhibiting greater stiffness improvements relative to the unreinforced specimen (CFST-X), as shown in Fig. 11. The average initial elastic stiffness enhancement index of specimens CFST-SS18 and CFST-DS18 increased by 63% and 36%, respectively, compared to specimen CFST-X. These results indicate that SPR inclusion fundamentally modifies the initial load transfer mechanism between the steel tube and concrete core. Unreinforced specimens (CFST-X) develop stress concentrations near the top region, reducing initial elastic stiffness. Conversely, the incorporation of SPR significantly modifies the composite action during the elastic phase. While a full confinement is typically delayed until the later stages, the embedded SPR instantaneously increases the overall effectively confined concrete area, contributing directly to the section's axial stiffness. Furthermore, the SPR augments the structural integrity of the steel tube walls and improves the restraint of the lateral expansion of the concrete core. This delay is implicitly supported by the delayed initiation of significant lateral strains observed in Fig. 10, suggesting a postponement of concrete microcracking relative to the unreinforced (CFST-X) specimens. Interestingly, the single SPR specimen (CFST-SS18) demonstrated higher average initial elastic stiffness than the double SPR specimen (CFST-DS18), suggesting a non-linear relationship with reinforcement quantity. This outcome is likely linked to constructability challenges associated with the denser double SPR arrangement within the small 100 mm × 100 mm cross-section. The restricted internal space in CFST-DS18 impeded the flow of fresh concrete, hindering adequate consolidation and vibration. This likely

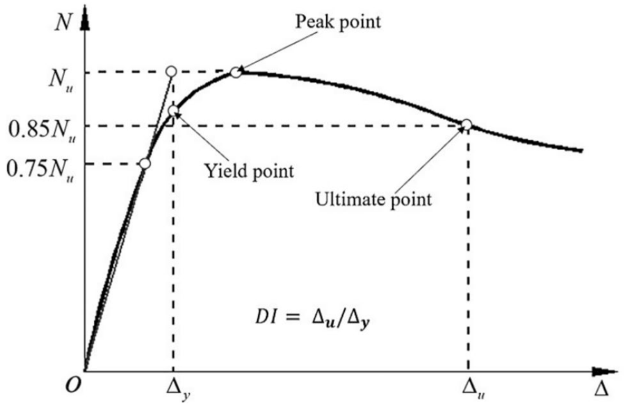

Fig. 12 Definition of ductility index (Zhao et al., 2022)

reduced the bonding efficiency at the steel-concrete interface, resulting in a marginal reduction of the elastic composite stiffness despite the increased steel area. This suggests that increasing the SPR quantity does not necessarily lead to an improvement in the initial elastic stiffness.

Ductility

In order to measure the effect of SPR on section ductility, this study employs the ductility index (*DI*), a widely recognized metric extensively documented in prior research (Abdullah et al., 2018; Huang et al., 2020; Yu et al., 2024). *DI* is mathematically defined as follows:

$$DI = \frac{\Delta_u}{\Delta_y} \tag{3}$$

In this equation, Δ_u represents the displacement corresponding to a load reduction to 85% of the peak value during the post-peak phase of the load–displacement curve. Meanwhile, Δ_y is determined using the secant stiffness method, which connects the origin to a point at 75% of the peak load magnitude, as detailed in prior studies (Ling et al., 2023; Park, 1988) and illustrated in Fig. 12. Δ_u and Δ_y can be determined from the axial load–displacement curves shown in Fig. 8.

To assess the ductility enhancement achieved through SPR, the ductility enhancement index (*DEI*) was utilized. This metric represents the ductility ratio of reinforced specimens to equivalent unreinforced specimens, given by:

$$DEI = \frac{DI_{SPR}}{DI_0} \tag{4}$$

where DI_{SPR} corresponds to the ductility index of specimen with SPR, whereas DI_0 denotes the ductility index of unreinforced specimen.

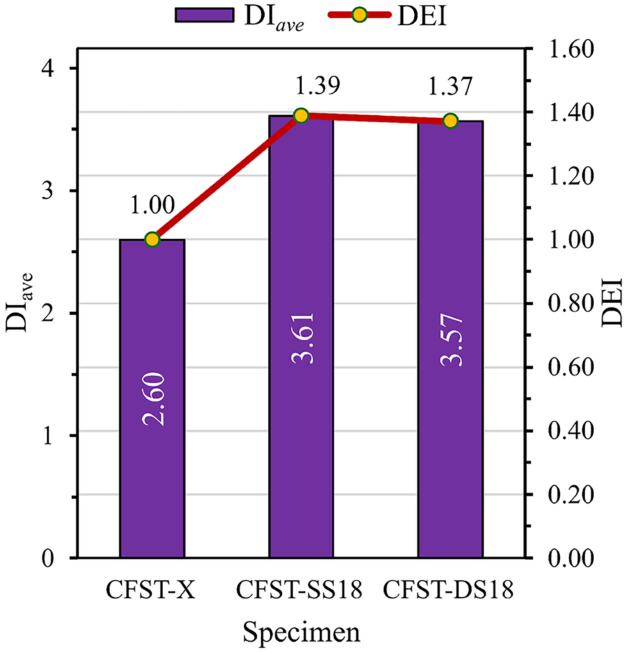

Fig. 13 Effect of SPR on the ductility of specimens

The confinement ratio, denoted as θ, is a key parameter for quantifying the confinement effect in CFST members. It is formally defined as the ratio of the axial load contribution of the steel tube to that of the concrete core as follows (Zhu et al., 2023)

$$\theta = \frac{A_a f_{y,st} + A_s f_{y,SPR}}{A_c f_c'} \tag{5}$$

where A_a, A_c, and A_s denote the cross-sectional area of the steel tube, the area of the infilled concrete and the area of the SPR, respectively. Similarly, $f_{y,st}$ represents the yield strength of the steel tube and $f_{y,SPR}$ signifies the yield strength of the SPR. The characteristic cylinder compressive strength (f_c') is derived using Equation 6, as proposed in Mirza and Lacroix (2004).

$$f_c' = f_{cu}[0.76 + 0.2\log_{10}\left(\frac{f_{cu}}{19.6}\right)] \tag{6}$$

where f_{cu} is the average cube compressive strength of concrete stated in Section 2.2.2.

Table 4 provides a summary of the *DI* and *DEI* values for all specimens. The average ductility index (DI_{ave}) and *DEI* are plotted in Fig. 13. As illustrated in Fig. 13, specimens incorporating SPR exhibited significantly higher ductility index compared to unreinforced specimens. This improvement is attributed to the SPR's role in providing lateral restraint to the concrete, thereby enhancing the steel-concrete interfacial interaction. Furthermore, Fig. 14(a) reveals

Fig. 14 Effects of confinement ratio on ductility and strength of specimen

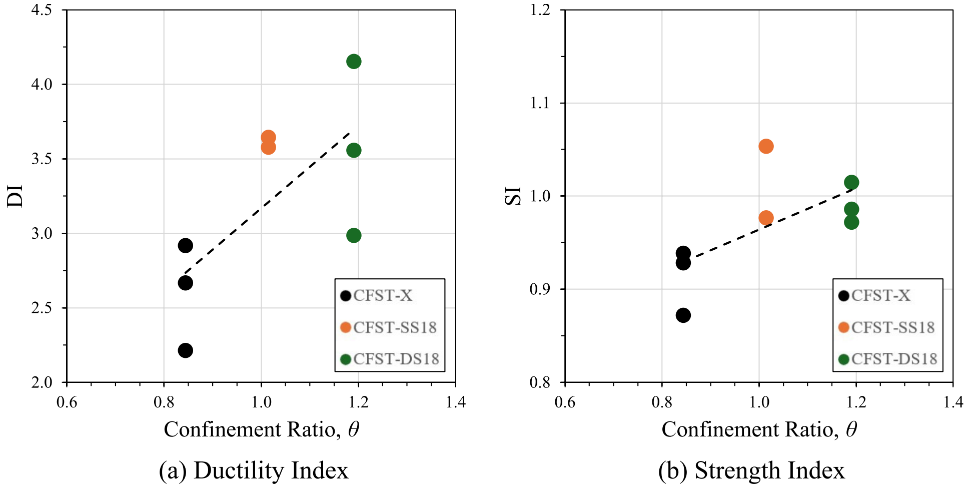

(a) Ductility Index

(b) Strength Index

a clear positive correlation between the confinement ratio (θ) and the ductility index (*DI*), confirming that increased in SPR generally leads to a more ductile structural response. While both reinforced configurations showed marked improvements, DI_{ave} for the double SPR specimens (CFST-DS18) was marginally lower than that of the single SPR specimens (CFST-SS18), with respective increases of 37% and 39% over the control group. The marginally lower *DI* observed in the double SPR specimens compared to the single SPR specimens can be attributed to differences in confinement effectiveness in square CFST sections. While the double SPR configuration further reduces the ineffective confinement zones and enhances axial strength, it subdivides the flat steel tube walls into shorter and stiffer restrained segments. This increased restraint limits of the steel tube walls and promotes localized strain concentration near the SPR concrete interfaces. In short square CFST columns, such localized restraint may lead to earlier concrete cracking, reducing the extent of progressive deformation after peak load. In contrast, the single SPR configuration allows greater deformation of the steel tube walls, facilitating a more gradual redistribution of stresses and progressive damage development in the concrete core. Consequently, despite providing stronger confinement and higher strength, the double SPR configuration exhibits a marginally lower deformation ductility, indicating the presence of an optimal SPR configuration for ductility enhancement in square CFST short columns.

Ultimate axial compressive strength

This section examines the influence of SPR on the ultimate axial compressive strength (N_u) of square CFST short column specimens. The strength enhancement due to SPR is quantified using the ultimate axial strength enhancement index (*UEI*), defined as:

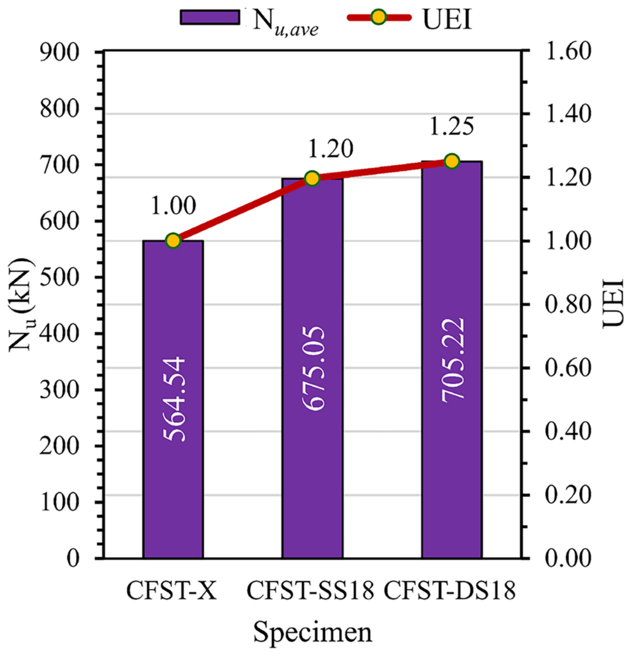

Fig. 15 Effect of SPR on the ultimate axial compressive strength of specimens

$$UEI = \frac{N_{u,SPR}}{N_{u,0}} \tag{7}$$

where $N_{u,SPR}$ and $N_{u,0}$ denote the ultimate axial compressive strength of square CFST short columns with SPR and unreinforced specimens, respectively.

Table 4 presents the ultimate axial compressive strength (N_u) and the ultimate axial compressive strength enhancement index (*UEI*) for specimens with and without SPR. Figure 15 further visualizes the average ultimate axial compressive strength ($N_{u,ave}$) measurements across tested groups. The results indicate that specimens with SPR exhibit markedly higher ultimate axial compressive strength values than unreinforced specimens, as evidenced by both tabulated data and graphical trends. The average enhancement observed was approximately 22%. These enhancements are attributed to the addition of SPR, a reinforcement mechanism that restrains the lateral expansion of the concrete core. Moreover, stresses within the ineffectively confined concrete area are redistributed, enabling the column to sustain a greater load. This restraint of lateral expansion, combined with the reduced ineffectively confined area, suppresses concrete crushing and consequently delays local buckling of the steel tube. Figure 15 demonstrates that $N_{u,ave}$ rises proportionally with the SPR configuration. Relative to CFST-X, specimens CFST-SS18 and CFST-DS18 exhibited ultimate axial compressive strength increases of 20% and 25%, respectively. It is observed that while doubling the reinforcement (DS18) provided the highest overall strength, the incremental increase over the single reinforcement (SS18) was approximately 5%. This suggests a point of diminishing returns where the theoretical strength gain from additional SPR area is partially offset by the increased congestion within the steel tube. As noted in Section 3.4.1, the denser arrangement of the double SPR restricts concrete flow and consolidation, preventing the composite section from fully capitalizing on the additional steel confinement.

Strength index

The steel tube restricts lateral expansion of the concrete core, thereby enhancing axial compressive strength. Incorporating SPR delays the initiation and propagation of local buckling in the steel tubes, which strengthens composite behavior. To quantify the confining effect of steel tubes on the concrete core, the strength index (*SI*) is commonly used (Tao et al., 2008; Wang et al., 2022). This parameter is a dimensionless quantity that is defined as follows:

$$SI = \frac{N_u}{A_a f_{y,st} + A_c f'_c + A_s f_{y,SPR}} \tag{8}$$

The denominator in Equation 8 corresponds to the cross-sectional capacity of the composite cross-section. The characteristic cylinder compressive strength (f'_c) is calculated using Equation 6.

Table 4 details the calculated *SI* values for all specimens. The results indicate *SI* values ranging from 0.872 to 1.053, suggesting effective composite interactions among the specimens. These interactions enhance load transfer mechanisms, strengthening the column's ultimate axial compressive strength. The CFST-X specimen without SPR exhibited average strength index SI_{ave} lower than unity, the lowest value among all tested configurations. As evidenced in Table 4, incorporating SPR significantly increased SI_{ave} values, confirming its role in amplifying composite interactions. This finding is further supported by Fig. 14(b), which illustrates a clear positive correlation between the confinement ratio (θ) and the strength index (*SI*). This improvement highlights the synergistic interaction between the steel tube and concrete core, facilitated by the integration of SPR. These findings also suggest that the confinement effect exerted by the steel tube on specimen CFST-X was comparatively weaker than in other specimens. Notably, the *SI* value for specimen CFST-SS18-2 was excluded from SI_{ave} of the CFST-SS18 group due to insufficient compaction of the concrete infill during fabrication. In contrast, SI_{ave} indicates that SPR effectively delays local buckling in the steel tube, thereby amplifying confinement effects.

Energy absorption

The energy absorption capacity of square CFST columns is quantified by integrating the axial load displacement curve. While commonly employed as a key indicator in seismic performance assessment, under monotonic axial loading this metric is used as a complementary indicator of axial toughness and post-peak deformation capacity, reflecting the specimen's ability to sustain load and deformation beyond peak strength. Pre-peak energy absorption (EA_{pre}) equals the area beneath the curve until attaining ultimate axial strength (N_u), while post-peak energy absorption (EA_{post}) corresponds to the area from peak load to 20 mm displacement. The total energy absorption (EA_t) represents the summation of EA_{pre} and EA_{post}. These calculated values for all tested specimens are detailed in Table 4. The corresponding average values are illustrated in Fig. 16.

Among the tested specimens, CFST-X displays notably lower total energy absorption, reflecting restricted energy absorption capacity. These findings highlight the substantial improvement in energy absorption achieved through SPR. The reinforced configurations, CFST-SS18 and CFST-DS18, showed enhanced performance with average pre-peak energy absorption ($EA_{pre,ave}$) increasing by 24% to 50%, post-peak energy absorption ($EA_{post,ave}$) by 24% to 34% and total energy absorption ($EA_{t,ave}$) by 24% to 36% relative to the unreinforced specimens. From a relative perspective, the energy absorption capacity in the pre-peak stage exhibits considerable sensitivity to the presence of SPR. However, in terms of absolute energy contribution, the enhancement is substantially more pronounced during the post-peak phase. The incorporation of a double SPR configuration contributed approximately 2500 Joules to the post-peak energy capacity. This value contrasts markedly with a contribution of only 531 Joules observed in the pre-peak stage. The observed enhancement suggests that incorporating SPR significantly enhances not only the axial

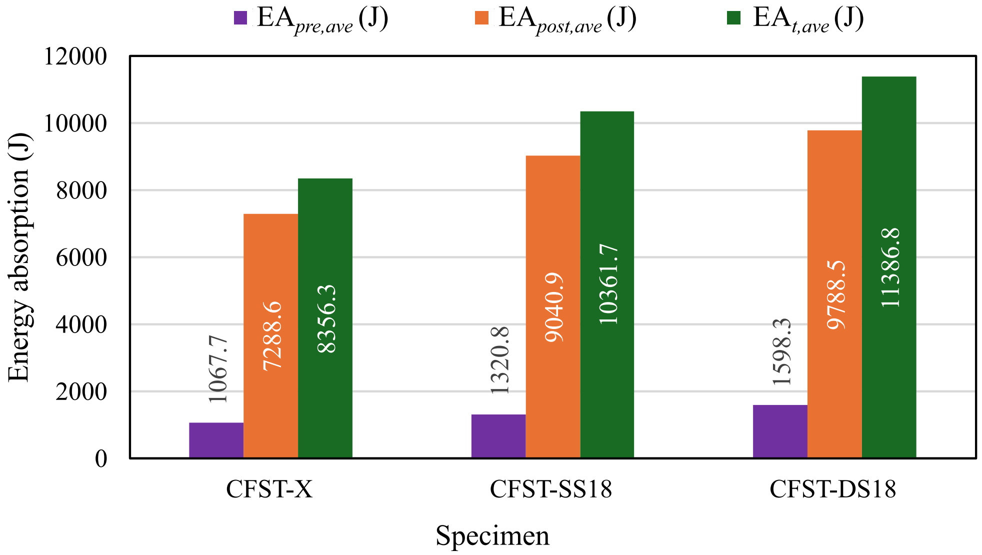

Fig. 16 Effect of SPR on the energy absorption capacities of specimen

compressive strength of the columns themselves but also their post-peak deformation performance. This improved energy absorption is linked to the confinement effect induced by SPR, which delays structural failure and facilitates greater deformation in the specimens.

Design recommendations

General

Current design codes primarily cover axially loaded CFST with conventional cross-sections, including circular, rectangular and square configurations. The square CFST short columns investigated in this study feature internal SPR, distinguishing them from standard sections. This study assesses axial compressive load capacity specified in EN 1994-1-1 (European Committee for Standardization, 2004), ANSI/AISC 360-22 (American Institute of Steel Construction, 2022), GB 50936-2014 (Ministry of Housing and Urban-Rural Development of the People's Republic of China, 2014) and AIJ (Architectural Institute of Japan, 1997) for square CFST short columns with SPR. New design equations derived from experimental results address limitations in existing design codes.

EN 1994-1-1

EN 1994-1-1 (European Committee for Standardization, 2004) establishes design methodologies for structural elements combining steel and concrete, such as composite columns. This standard governs structural steel grades from S235 to S460 and normal weight concrete within strength classes C20/25 to C50/60. For rectangular or square CFST sections, a concrete coefficient of 1.0 applies. The axial compressive load capacity equation for square CFST column based on EN 1994-1-1, denoted as N_{EC4}, accounts for combined contributions from steel, concrete and reinforcement as follows:

$$N_{EC4} = A_a f_{y,st} + A_c f_c' + A_s f_{y,SPR} \tag{9}$$

Equation 9 applies to square CFST sections complying with the slenderness limit outlined in the standard. When this limit is surpassed, local buckling of the steel tube can develop its yield strength. Consequently, when the section slenderness ($\lambda = H/t$) exceeds the limit value of $52\sqrt{235/f_{y,st}}$, the effective width method stipulated in EN 1993-1-5 (European Committee for Standardization, 2006) must be employed. This method calculates the reduction factor ρ using the following expression:

$$\rho = (1 - 0.22/\bar{\lambda}_p)/\bar{\lambda}_p \tag{10}$$

where $\bar{\lambda}_p$ denotes the steel slenderness, defined as $\bar{\lambda}_p = \sqrt{f_{y,st}/f_{cr}}$. Here, f_{cr} represents the critical elastic buckling stress of the steel tube. This stress is determined from steel buckling theory using the following expression:

$$f_{cr} = k\frac{\pi^2 E_s}{12(1-\nu^2)(H/t)^2} \tag{11}$$

where E_s is the Young's modulus of the steel tube, ν is Poisson's ratio of the steel tube and k is the steel buckling coefficient, typically assigned a value of 4. The reduction factor ρ is subsequently used to compute the effective area of the square steel tube. Previous studies on square and circular section CFST columns, as well as double skin tubular short columns, have employed similar strength reduction approach (Li et al., 2025; Su et al., 2020; Wang et al., 2019).

ANSI/AISC 360-22

According to ANSI/AISC 360-22 (American Institute of Steel Construction, 2022), the design code is applicable to structural steel with yield strengths up to 690 MPa and concrete with cylindrical compressive strengths ranging between 21 MPa and 100 MPa. This standard classifies CFST column cross-sections into compact, non-compact or slender types based on the slenderness ratio of the steel tube ($\lambda = H/t$). All specimens examined in this study meet the requirements for compact sections as defined by this classification.

Compact sections are defined by a slenderness ratio $\lambda \le \lambda_p = 2.26\sqrt{E_s/f_{y,st}}$ for square section,

$$N_{ANSI} = N_p = A_a f_{y,st} + 0.85 f_c' \left(A_c + A_s \frac{E_s}{E_{c,ANSI}} \right) \tag{12}$$

where λ_p denotes the slenderness ratio limit demarcating compact and noncompact sections and N_p represents the compressive strength of compact sections. $E_{c,ANSI}$ is the corresponding elastic modulus of concrete, calculated as follows:

$$E_{c,ANSI} = 0.043 w_c^{1.5} \sqrt{f_c'} \tag{13}$$

where w_c represents the weight of concrete per unit volume, conventionally ranging from 1500 to 2500 kg/m^3.

GB 50936-2014

GB 50936-2014 (Ministry of Housing and Urban-Rural Development of the People's Republic of China, 2014) outlines design equations for CFST columns with various cross-sectional geometries. This standard covers structural steel grades from Q235 ($f_y = 235$ MPa) to Q420 ($f_y = 420$ MPa) and concrete grades from C30 ($f_{ck} = 20.1$ MPa) to C80 ($f_{ck} = 50.2$ MPa). For square CFST sections, the standard imposes a cross-sectional slenderness limit of $H/t \le 60\sqrt{235/f_{y,st}}$ to prevent the effect of local buckling. The axial compressive load capacity equation, denoted as N_{GB}, is determined according to the following equation:

$$N_{GB} = (1.212 + B\xi + C\xi^2)(A_s + A_c) f_{ck} + A_s f_{sk} \tag{14}$$

In this context, f_{ck} denotes the characteristic compressive strength of concrete. This property is determined from prism specimens measuring 150 mm × 150 mm × 300 mm. The value of f_{ck} may be derived from the compressive cube strength (f_{cu}) which is obtained from 150 mm × 150 mm × 150 mm cubes. The relationship between f_{ck} and f_{cu} is specified in GB 50936-2014 as follows:

$$f_{ck} = 0.88 \alpha_1 \alpha_2 f_{cu} \tag{15}$$

The factor α_1 represents the reduction accounting for differences in concrete strength between standardized test specimens and actual structural elements. For the concrete grade lower than C50, α_1 is taken as 0.76. Meanwhile, α_2 denotes the reduction factor addressing concrete brittleness effects. This factor adopts values of 1.0 for concrete grade lower than C40 concrete.

The term ξ in Equation 14 denotes the confining factor. This parameter can be calculated using the following equation:

$$\xi = \frac{A_a f_{y,st}}{A_c f_{ck}} \tag{16}$$

Parameters B and C in Equation 14 account for confinement effects that vary with cross-sectional geometry. For square CFST sections, these parameters are determined as follows:

$$B = \frac{0.131 f_{y,st}}{213} + 0.723 \tag{17}$$

$$C = -\frac{0.070 f_{ck}}{14.4} + 0.026 \tag{18}$$

When section slenderness exceeds the prescribed limit of $60\sqrt{235/f_{y,st}}$, GB 50936-2014 does not provide any design equations. Consequently, this study applies the identical effective width methodology specified in EN 1994-1-1 (Section 4.2) to compute the steel tube's effective cross-sectional area. This calculated effective area substitutes the original steel area, A_s in Equation 14, thereby modifying the CFST axial compressive load capacity.

AIJ

The axial compressive load capacity provided by AIJ (Architectural Institute of Japan, 1997) for the resistance of the square CFST short columns with SPR is given as Equation 19 as below. AIJ specifies concrete strengths ranging from 18 MPa to 90 MPa and steel strengths between 235 MPa and 440 MPa.

$$N_{AIJ} = A_a f_{y,st} + 0.85 A_c f_c' + A_s f_{y,SPR} \tag{19}$$

While similar to the EN 1994-1-1 axial compressive load capacity formulation, Equation 19 incorporates a distinct

0.85 reduction coefficient for concrete and a higher *H*/*t* limit of $72\sqrt{235/f_y}$.

Assessment of existing design codes

Sections 4.2–4.5 present the design equations from EN 1994-1-1, ANSI/AISC 360-22, GB 50936-2014 and AIJ, which are evaluated against the experimental results. All four existing design codes require evaluating the steel tube for potential local buckling before yielding, typically based on its slenderness limits. The slenderness limits in ANSI/AISC 360-22 and AIJ were not exceeded in this study, allowing direct application of their respective design equations without reduction factors. However, the EN 1994-1-1 and GB 50936-2014 slenderness limit was exceeded, requiring a reduction factor to address potential steel tube local buckling. Local buckling evaluation is not required for the internal SPR, as it remains fully restrained by the surrounding concrete, preventing instability.

Table 5 compares the experimentally obtained ultimate axial compressive strength (N_u) with predictions from existing design codes for square CFST short columns with SPR. The performance of N_u is evaluated against each design code using statistical parameters such as mean, standard deviation (SD) and coefficient of variation (CoV). EN 1994-1-1 yields a mean N_u/N_{EC4} value of 1.104, with an SD of 0.057 and a CoV of 0.052. This reflects a consistent conservative trend, where the experimentally measured strengths exceed the predicted capacities. The ANSI/AISC 360-22 code shows a similar trend with a mean ratio of 1.086, SD of 0.084 and a CoV of 0.077, indicating a greater variability and lower precision in its predictions compared to EN 1994-1-1. Conversely, GB 50936-2014 produces a mean ratio of 0.936 (SD = 0.054, CoV = 0.058), suggesting slight non-conservatism where the code overestimates axial compressive load capacity. This tendency may present safety implications in design practice. The AIJ method achieves a mean ratio of 1.045, SD of 0.056 and CoV of 0.053, demonstrating balanced performance with modest conservatism and consistent accuracy.

Generally, the abovementioned design codes provide reasonable predictions of axial compressive load capacity for square CFST short column with SPR. However, EN 1994-1-1 demonstrates greater conservatism, whereas GB 50936-2014 tended to overestimate the axial compressive load capacity, indicating a non-conservative approach. This disparity is attributed to requirement for a reduction factor when the section slenderness surpasses its prescribed limit, which occurred for the specimens in this study. This adjustment for potential local buckling results in a further decrease in predicted axial compressive load capacity, rendering EN 1994-1-1 particularly conservative whereas GB 50936-2014 non-conservative under these conditions. To enhance the accuracy of axial compressive load capacity predictions, new design equations have been proposed by more accounting for the steel concrete interaction and the confinement effect provided by the SPR within the steel tube.

Proposed predictive equation

This research proposes new design equations for square CFST short columns incorporating internal SPR. A fundamental principle in CFST column design involves the steel tube-concrete core interaction. During initial elastic response under axial loading, interfacial contact remains limited due to steel's higher Poisson ratio compared to concrete. As loading intensifies and concrete develops lateral expansion through cracking, interaction initiates between the concrete core and steel tube. This engagement prompts the steel tube to develop lateral confinement, inducing a

Table 5 Comparison between the experimental results and existing design methods

Specimen	N_u (kN)	EN 1994-1-1		ANSI/AISC 360-22		GB 50936-2014		AIJ		Proposed Approach	
		N_{EC4} (kN)	N_u/N_{EC4}	N_{ANSI} (kN)	N_u/N_{ANSI}	N_{GB} (kN)	N_u/N_{GB}	N_{AIJ} (kN)	N_u/N_{AIJ}	N_{prop} (kN)	N_u/N_{prop}
CFST-X-1	574.0	536.3	1.070	568.2	1.010	640.4	0.896	568.2	1.010	602.7	0.952
CFST-X-2	539.2	536.3	1.005	568.2	0.949	640.4	0.842	568.2	0.949	602.7	0.895
CFST-X-3	580.4	536.3	1.082	568.2	1.021	640.4	0.906	568.2	1.021	602.7	0.963
CFST-SS18-1	649.6	583.0	1.114	592.5	1.096	687.7	0.945	615.7	1.055	659.5	0.985
CFST-SS18-2	517.6	583.0	-[1]	592.5	-[1]	687.7	-[1]	615.7	-[1]	659.5	-[1]
CFST-SS18-3	700.6	583.0	1.202	592.5	1.182	687.7	1.019	615.7	1.138	659.5	1.062
CFST-DS18-1	691.8	629.7	1.099	616.8	1.122	734.9	0.941	663.2	1.043	713.0	0.970
CFST-DS18-2	722.1	629.7	1.147	616.8	1.171	734.9	0.983	663.2	1.089	713.0	1.013
CFST-DS18-3	701.7	629.7	1.114	616.8	1.138	734.9	0.955	663.2	1.058	713.0	0.984
Mean	-	-	1.104	-	1.086	-	0.936	-	1.045	-	0.978
SD	-	-	0.057	-	0.084	-	0.054	-	0.056	-	0.048
CoV	-	-	0.052	-	0.077	-	0.058	-	0.053	-	0.049

[1] Result is not included because of poor concrete compaction

triaxial compression state in the concrete. The axial compressive load capacity proposed for these square CFST short columns with SPR is determined by the following equation:

$$N_{prop} = A_a\sigma_{yv} + A_c f_{cc} + A_s\sigma_{sv} \tag{20}$$

where σ_{yv} and σ_{sv} represent the longitudinal stresses in the steel tube and the SPR, respectively. The term f_{cc} denotes the modified confined compressive strength of the infilled concrete core. This parameter is calculated according to the method proposed by Cusson and Paultre (1994), but the form shown in Equation 21 is taken from Thomas and Sandeep (2020).

$$f_{cc} = f_c' + k_e f_l' \tag{21}$$

where f_l' signifies the confining pressure applied by the steel tube to the core concrete, determined using Equation 25. The term f_c' represents the characteristic cylinder compressive strength of the concrete obtained from Equation 6 presented in this study. According to Mander et al. (1988) and Shen et al. (2022), the confinement effectiveness coefficient is represented by k_e. The cross-sectional areas of the effectively confined and ineffectively confined concrete core are designated as A_{ce} and A_{cv}, respectively. These parameters are defined in equations 22–24.

$$k_e = \frac{A_{ce}}{A_c} \tag{22}$$

$$A_{ce} = A_c - A_{cv} \tag{23}$$

$$A_{cv} = \sum_{i=1}^{n} \frac{w_i^2}{6} \tag{24}$$

where n denotes the number of ineffectively confined concrete core zones. The boundaries separating effectively confined and ineffectively confined areas are demarcated by second-order parabolic curves. These curves initiate and terminate at 45-degree angles, as illustrated in Fig. 17. Within the defined coordinate system, the second-order parabolic curve on the right side of the origin is expressed as $y = -(x^2/w_i) + w_i/4$. The area corresponding to a single curve and the steel tube boundaries is $w_i^2/6$.

The confining effect provided by the SPR on the steel tube can be expressed as an equivalent force. Based on force equilibrium at the steel-concrete interface, illustrated in Fig. 18, the horizontal force equilibrium is expressed by the following equation.

$$2\sigma_{yh}t + \sum_{i=1}^{n_{SPR}} \sigma_{sh}t_{SPR} = f_l'(B - 2t) \tag{25}$$

where σ_{yh} and σ_{sh} represent the horizontal stresses in the steel tube and the SPR, respectively. The term n_{SPR} represents the number of SPR on each side of the steel tube wall.

Experimental results demonstrate that all specimens incorporating SPR failed in post-local buckling mode. The steel yielded as these columns attained their ultimate strength, satisfying the Von Mises criterion expressed by:

$$\sigma_{yh}^2 - \sigma_{yh}\sigma_{yv} + \sigma_{yv}^2 = f_{y,st}^2 \tag{26}$$

$$\sigma_{sh}^2 - \sigma_{sh}\sigma_{sv} + \sigma_{sv}^2 = f_{y,SPR}^2 \tag{27}$$

As established by Sakino et al. (2004), σ_{sh} and σ_{sv} are expressed as follows:

$$\sigma_{sh} = 0.19 f_{y,SPR} \tag{28}$$

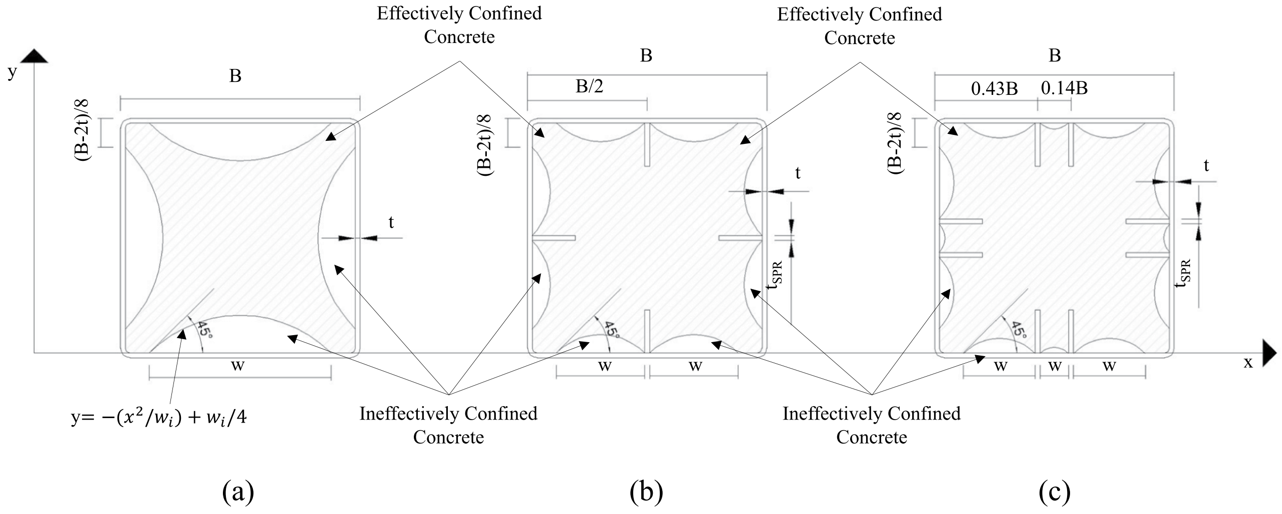

Fig. 17 Confinement region distribution patterns for specimens: **a** Unreinforced, **b** Single SPR, **c** Double SPR

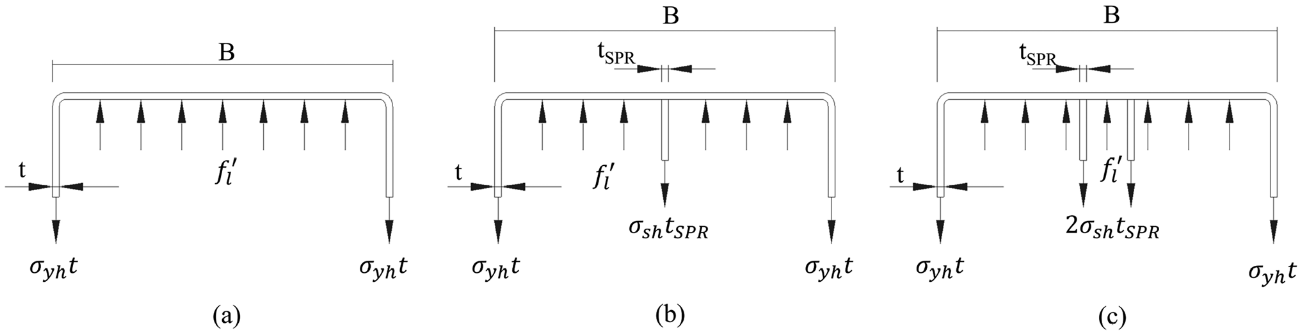

Fig. 18 Lateral confinement of concrete core: **a** Unreinforced, **b** Single SPR, **c** Double SPR

$$\sigma_{sv} = 0.89f_{y,SPR} \tag{29}$$

Current design codes including EN 1994-1-1 and GB 50936-2014 specify conservatively restricted slenderness limits. Chen et al. (2021) demonstrate through experimental validation that these limits can be safely increased to $68\sqrt{235/f_y}$, without compromising structural performance. By integrating this limit with experimental data, it can be used to evaluate the effective strengthening effect of the SPR on the steel tube. Consequently, the horizontal and longitudinal stresses (σ_{yh} and σ_{yv}) in the steel tube can be calculated.

When $\frac{B}{t_{SPR}} > 68\sqrt{235/f_{y,SPR}}$, local buckling of the steel tube prior to attaining ultimate strength becomes a significant consideration. Ge and Usami (1992) established the following relationship to address this behavior:

$$R = \frac{B}{t}\sqrt{\frac{12(1-\nu_{SPR}^2)}{4\pi^2}}\sqrt{\frac{f_{y,st}}{E_s}} \tag{30}$$

where R and ν_{SPR} denotes the width-to-thickness ratio parameter and Poisson's ratio of the SPR, respectively.

Based on the Von Mises criterion, Cai and He (2006) derived expressions for σ_{yv} and σ_{yh} as follows:

$$\sigma_{yv} = \left(\frac{1.2}{R} - \frac{0.3}{R^2}\right) f_{y,st} \tag{31}$$

$$\sigma_{yh} = \left(\sigma_{yv} - \sqrt{4f_{y,st}^2 - 3\sigma_{yv}^2}\right)/2 \tag{32}$$

When $\frac{B}{t_{SPR}} \leq 68\sqrt{235/f_{y,SPR}}$, local buckling of the steel tube prior to reaching ultimate strength may be disregarded. Hence, σ_{yh} and σ_{yv} can be defined as:

$$\sigma_{yh} = 0.19f_{y,st} \tag{33}$$

$$\sigma_{yv} = 0.89f_{y,st} \tag{34}$$

Table 5 compares predictions from the proposed equations with experimental results. The N_u/N_{prop} ratio demonstrates close agreement, yielding a mean of 0.978, SD of 0.048 and CoV of 0.049. The findings confirm that the proposed equations provide improved predictions of axial compressive load capacity of square CFST short columns with SPR compared to current design codes. The proposed equations were derived and validated using experimental results from this study, which cover a defined parameter range. A complementary numerical study examining confinement mechanisms and internal stress distributions is currently in progress.

Conclusion

This study presented an experimental investigation into the axial compressive behavior of square CFST short columns internally reinforced with Steel Plate Reinforcement (SPR). Based on the results and analysis, the following conclusions are drawn:

1. The integration of SPR effectively delayed the onset of local buckling and shifted the failure location from the column ends to the mid-height region. This shift indicates a more uniform stress distribution and enhanced confinement of the concrete core. While all specimens failed through steel tube local buckling and concrete crushing, specimens with SPR demonstrated significantly improved post-peak stability compared to unreinforced counterparts.
2. The inclusion of SPR consistently enhanced the fundamental mechanical properties of the columns. Compared to unreinforced specimens, the SPR configurations increased initial elastic stiffness by up to 63%, ductility by up to 39%, ultimate axial strength by up to 25% and total energy absorption by up to 36%. Notably, while the double SPR configuration (CFST-DS18) provided the highest strength and energy absorption, the single SPR configuration (CFST-SS18) yielded slightly

superior ductility, indicating an optimal reinforcement density for deformation capacity.

3. An assessment of existing design codes revealed that EN 1994-1-1, ANSI/AISC 360-22 and AIJ provides conservative predictions, whereas GB 50936-2014 tends to be non-conservative for these specific sections. To address this, a new design equation accounting for the SPR confinement effect was proposed. The proposed equation demonstrates strong agreement with experimental results (mean N_u/N_{prop} of 0.978 and CoV of 0.049), offering a reliable prediction method for square CFST columns with SPR.

Acknowledgements The authors acknowledged the financial support from the Ministry of Higher Education Malaysia through Fundamental Research Grant Scheme (FRGS), FRGS/1/2023/TK06/UNIMAS/02/1 and Universiti Malaysia Sarawak for supporting this project.

Author contributions Writing - Original Draft: A. C. W.; Writing - Review & Editing: A. A. A., A. R. A. K., A. B. H. K., B. G. B.; Investigation: A. C. W., B. G. B.; Visualization: A. C. W.; Funding acquisition: A. A. A.; Supervision: A. A. A., A. R. A. K.;

Funding Open access funding provided by The Ministry of Higher Education Malaysia and Universiti Malaysia Sarawak

Data availability No datasets were generated or analysed during the current study.

Materials availability Not applicable

Code availability Not applicable

Declarations

Conflict of interest The authors declare no Conflict of interest.

References

Abdullah, A. A., Mutalib, A. A., Baharom, S., & Badaruzzaman, W. H. W. (2018). Mechanical behavior of square cfst columns with embedded steel plate reinforcement. *International Journal of Structural and Civil Engineering Research, 7*, 319–322. https://doi.org/10.18178/ijscer.7.4.319-322

Abdullah, A. A., Mutalib, A. A., Baharom, S., & Badaruzzaman, W. H. W. (2020). Parametric study on the influence of embedded spr to the performance of square cfst columns. *International Journal of Integrated Engineering, 12*, 191–198.

Abramski, M. (2018). Load-carrying capacity of axially loaded concrete-filled steel tubular columns made of thin tubes. *Archives of Civil and Mechanical Engineering, 18*, 902–913. https://doi.org/10.1016/j.acme.2018.01.002

Ahmed, A. D., & Güneyisi, E. M. (2019). Structural performance of frames with concrete-filled steel tubular columns and steel beams: Finite element approach. *Advanced Composites Letters,28*,. https://doi.org/10.1177/2633366X19894593

Alatshan, F., Osman, S. A., Altlomate, A., Alkair, M., Hamid, R., & Mashiri, F. (2023). Design model of rectangular concrete-filled steel tubular stub columns under axial compression. *Buildings, 13*(1), 128. https://doi.org/10.3390/buildings13010128

Alatshan, F., Osman, S. A., Hamid, R., & Mashiri, F. (2020). Stiffened concrete-filled steel tubes: A systematic review. *Thin-Walled Structures, 148*, Article 106590. https://doi.org/10.1016/j.tws.2019.106590

American Institute of Steel Construction (2022). Specification for structural steel buildings (ansi/aisc 360–22) (ANSI/AISC 360–22 ed.). American Institute of Steel Construction.

Anilkumar, A., & Kavitha, P.E. (2020). Numerical analysis of windowed steel tube embedded in concrete. In (p. 323–333).

Architectural Institute of Japan (1997). Recommendations for design and construction of concrete filled steel tubular structures.

Ayough, P., Ibrahim, Z., Sulong, N. H. R., Ganasan, R., Ghayeb, H. H., & Elchalakani, M. (2022). Experimental and numerical investigations into the compressive behaviour of circular concrete-filled double-skin steel tubular columns with bolted shear studs. *Structures, 46*, 880–898. https://doi.org/10.1016/j.istruc.2022.10.102

Bhatia, S., & Tiwary, A.K. (2023). Behaviour of concrete filled single skinned steel tube columns subjected to different loading states. (p. 020076).

Cai, J., & He, Z.-Q. (2006). Axial load behavior of square cft stub column with binding bars. *Journal of Constructional Steel Research, 62*, 472–483. https://doi.org/10.1016/j.jcsr.2005.09.010

Cai, J., & Long, Y.-L. (2007). Axial load behavior of rectangular cft stub columns with binding bars. *Advances in Structural Engineering, 10*, 551–565. https://doi.org/10.1260/136943307782417663

Chang, Z. H., Azmi, M. R., & Yatim, M. Y. M. (2024). Ultimate strength and design of cfdst columns with intermittent welded plate stiffeners. *Journal of Constructional Steel Research, 218*, Article 108689. https://doi.org/10.1016/j.jcsr.2024.108689

Chen, J., Chan, T.-M., & Chung, K.-F. (2021). Design of square and rectangular cfst cross-sectional capacities in compression. *Journal of Constructional Steel Research, 176*, Article 106419. https://doi.org/10.1016/j.jcsr.2020.106419

Chen, S., Ahmed, M., Ci, J., Chen, W., & Sennah, K. (2022). Behavior and design of axially loaded square concrete-filled double steel tubular slender columns. *Advances in Structural Engineering, 25*, 2953–2965. https://doi.org/10.1177/13694332221113041

Ci, J., Kong, L., Ahmed, M., Liang, Q. Q., Hamoda, A., Chen, S., & Wu, C. (2022). Experimental and numerical studies of axially loaded square concrete-encased concrete-filled large-diameter steel tubular short columns. *Structural Concrete, 23*, 2748–2769. https://doi.org/10.1002/suco.202100466

Cusson, D., & Paultre, P. (1994). High-strength concrete columns confined by rectangular ties. *Journal of Structural Engineering, 120*, 783–804. https://doi.org/10.1061/(ASCE)0733-9445(1994)120:3(783)

Debnath, P. P., Xu, F., & Chan, T.-M. (2023). Load transfer mechanism in concrete-filled steel tubular columns: Developments, challenges and opportunities. *Journal of Constructional Steel*

Research, 203, Article 107781. https://doi.org/10.1016/j.jcsr.2023.107781

Deng, Z., Hu, Q., Wang, W., & Xiong, M.-X. (2025). Compressive load-strain response of cfrp-stirrups reinforced high-strength cfst columns and a unified steel-frp confinement model. *Structures, 82*, Article 110728. https://doi.org/10.1016/j.istruc.2025.110728

Department of Standards Malaysia (2010). Ms en 1992-1-1:2010: Eurocode 2 - design of concrete structures - part 1–1: General rules and rules for buildings (Tech. Rep.). Department of Standards Malaysia. (Malaysian Standard adopted from European Standard EN 1992-1-1).

Department of Standards Malaysia (2012). Ms en 12390–3:2012: Testing hardened concrete - part 3: Compressive strength of test specimens (Tech. Rep.). Department of Standards Malaysia.

Diao, R., Hu, X., Xie, L., & Chen, Z. (2025). Evaluation of eccentric compressive behavior between active and passive preloading in cfst. *Applied Sciences, 15*, 2273. https://doi.org/10.3390/app15052273

Du, Y., Chen, Z., & Xiong, M.-X. (2016). Experimental behavior and design method of rectangular concrete-filled tubular columns using q460 high-strength steel. *Construction and Building Materials, 125*, 856–872. https://doi.org/10.1016/j.conbuildmat.2016.08.057

Elchalakani, M., Hassanein, M., Karrech, A., & Yang, B. (2018). Experimental investigation of rubberised concrete-filled double skin square tubular columns under axial compression. *Engineering Structures, 171*, 730–746. https://doi.org/10.1016/j.engstruct.2018.05.123

European Committee for Standardization (2004). Eurocode 4: Design of composite steel and concrete structures - part 1–1: General rules and rules for buildings (Tech. Rep.). European Committee for Standardization.

European Committee for Standardization (2006). Eurocode 3 en 1993-1-5:2006: Design of steel structures - part 1–5: Plated structural elements.

Gardner, L., & Yun, X. (2018). Description of stress-strain curves for cold-formed steels. *Construction and Building Materials, 189*, 527–538. https://doi.org/10.1016/j.conbuildmat.2018.08.195

Ge, H., & Usami, T. (1992). Strength of concrete-filled thin-walled steel box columns: Experiment. *Journal of Structural Engineering, 118*, 3036–3054. https://doi.org/10.1061/(ASCE)0733-9445(1992)118:11(3036)

George, C., Selvan, S. S., Kumar, V. S., Murali, G., Giri, J., Makki, E., & Sathish, T. (2024). Enhancing the fire-resistant performance of concrete-filled steel tube columns with steel fiber-reinforced concrete. *Case Studies in Construction Materials, 20*, Article e02741. https://doi.org/10.1016/j.cscm.2023.e02741

Guo, J., & Diao, Y. (2022). Experimental behaviors of square concrete filled steel tubular columns with pbl stiffeners. *Structures, 38*, 1556–1569. https://doi.org/10.1016/j.istruc.2022.03.003

Han, R., Zhao, H., Sun, Y., Ju, N., & Zhao, S. (2022). Cyclic behavior of concrete-filled square tubular columns with stiffened plastic hinge region. *Journal of Constructional Steel Research, 190*, Article 107152. https://doi.org/10.1016/j.jcsr.2022.107152

Hongsong, H. U., Kang, L. I. N., & Yang, L. I. U. (2019). Study on compressive strength of steel tube and concrete in square cft columns. *Journal of Building Structures, 40*, 161–168. https://doi.org/10.14006/j.jzjgxb.2019.02.015

Hossain, K. M., & Chu, K. (2019). Confinement of six different concretes in cfst columns having different shapes and slenderness. *International Journal of Advanced Structural Engineering, 11*, 255–270. https://doi.org/10.1007/s40091-019-0228-2

Hu, Y. M., Yu, T., & Teng, J. G. (2011). Frp-confined circular concrete-filled thin steel tubes under axial compression. *Journal of Composites for Construction, 15*, 850–860. https://doi.org/10.1061/(ASCE)CC.1943-5614.0000217

Huang, Y., Lu, Y., Ma, W., & Yan, Y. (2024). Experimental and numerical investigation on axial behavior of circular and square slender reinforced columns. *Journal of Constructional Steel Research, 213*, Article 108417. https://doi.org/10.1016/j.jcsr.2023.108417

Huang, Z., Uy, B., Li, D., & Wang, J. (2020). Behaviour and design of ultra-high-strength cfst members subjected to compression and bending. *Journal of Constructional Steel Research, 175*, Article 106351. https://doi.org/10.1016/j.jcsr.2020.106351

Huo, J., Huang, G., & Xiao, Y. (2009). Effects of sustained axial load and cooling phase on post-fire behaviour of concrete-filled steel tubular stub columns. *Journal of Constructional Steel Research, 65*, 1664–1676. https://doi.org/10.1016/j.jcsr.2009.04.022

International Organization for Standardization (2019). Iso 6892–1:2019: Metallic materials - tensile testing - part 1: Method of test at room temperature.

Islam, M. M., Ali, R. B., Begum, M., & Rahman, M. S. (2021). Experimental study of square concrete-filled welded cold-formed steel columns under concentric loading. *Arabian Journal for Science and Engineering, 46*, 4225–4237. https://doi.org/10.1007/s13369-020-04797-9

Kim, S.-H., Yom, K.-S., & Choi, S.-M. (2015). A study on the structural performance of new shape built-up square column under concentric axial load. *Steel and Composite Structures, 18*, 1451–1464. https://doi.org/10.12989/scs.2015.18.6.1451

Lai, B.-L., Li, Y.-R., Becque, J., Zheng, Y.-Y., & Fan, S.-G. (2025). Axial compressive behavior of circular stainless steel tube confined uhpc stub columns under monotonic and cyclic loading. *Thin-Walled Structures, 208*, Article 112830. https://doi.org/10.1016/j.tws.2024.112830

Lai, B. L., Li, Y. R., Jin, L., & Fan, S. G. (2024). Experimental study on the compressive behavior of uhpc filled stainless steel tubes subjected to monotonic and cyclic loading. *Construction and Building Materials, 449*, Article 138301. https://doi.org/10.1016/j.conbuildmat.2024.138301

Lai, B.-L., Li, Y.-R., Zhao, J.-H., Kong, Z.-Y., & Fan, S.-G. (2025). Experimental study on the interfacial bond behavior of uhpc filled circular stainless steel tubes. *Journal of Constructional Steel Research, 224*, Article 109172. https://doi.org/10.1016/j.jcsr.2024.109172

Le, H. A. (2023). Evaluation of confining pressure models for circular concrete-filled steel tube short columns under concentric loading. *Engineering, Technology & Applied Science Research, 13*, 10181–10185. https://doi.org/10.48084/etasr.5537

Lehman, D. E., & Roeder, C. W. (2012). Foundation connections for circular concrete-filled tubes. *Journal of Constructional Steel Research, 78*, 212–225. https://doi.org/10.1016/j.jcsr.2012.07.001

Li, S., Liu, F., Chan, T.-M., Yang, H., & Young, B. (2025). Novel concrete-filled steel square tubular columns stiffened with semi-circles: Concept and behaviour. *Thin-Walled Structures, 212*, Article 113188. https://doi.org/10.1016/j.tws.2025.113188

Liao, J., Zeng, J.-J., Quach, W.-M., & Zhou, J.-K. (2023). Axial compressive behavior and model assessment of frp-confined seawater sea-sand concrete-filled stainless steel tubular stub columns. *Composite Structures, 311*, Article 116782. https://doi.org/10.1016/j.compstruct.2023.116782

Liao, J. J., Zeng, J. J., Long, Y. L., Cai, J., & Ouyang, Y. (2022). Behavior of square and rectangular concrete-filled steel tube (cfst) columns with horizontal reinforcing bars under eccentric compression. *Engineering Structures, 271*, Article 114899. https://doi.org/10.1016/j.engstruct.2022.114899

Ling, J. H., Lim, Y. T., & Jusli, E. (2023). Methods to determine ductility of structural members: A review. *Journal of the Civil Engineering Forum, 9*, 181–194. https://doi.org/10.22146/jcef.6631

Liu, H. L., & Cai, J. (2013). Research on behavior of rectangular cfst stub columns with binding bars under axial compression. *Applied*

Mechanics and Materials, 351–352, 790–797. https://doi.org/10.4028/www.scientific.net/AMM.351-352.790

Ma, W., Yan, Y., Lu, Y., Li, S., & Wang, L. (2025). Axially loaded square cfst short columns strengthened with high-strength square steel tubes and concrete jackets. *Engineering Structures, 324*, Article 119395. https://doi.org/10.1016/j.engstruct.2024.119395

Mander, J. B., Priestley, M. J. N., & Park, R. (1988). Theoretical stress-strain model for confined concrete. *Journal of Structural Engineering, 114*, 1804–1826. https://doi.org/10.1061/(ASCE)0733-9445(1988)114:8(1804)

Megahed, K., Mahmoud, N. S., & Abd-Rabou, S. E. M. (2024). Finite element modeling for concrete-filled steel tube stub columns under axial compression. *International Journal of Steel Structures, 24*, 1229–1250. https://doi.org/10.1007/s13296-024-00896-7

Miao, K., Wei, Y., Zhang, S., Zheng, K., & Ding, M. (2023). Eccentric compression behavior of concrete-filled steel tube columns strengthened by cfrp/steel strip. *Engineering Structures, 287*, Article 116191. https://doi.org/10.1016/j.engstruct.2023.116191

Ministry of Housing and Urban-Rural Development of the People's Republic of China (2014). Gb 50936–2014: Code for design of concrete-filled steel tubular structures (Tech. Rep.). China Architecture & Building Press.

Mirza, S. A., & Lacroix, E. A. (2004). Comparative strength analyses of concrete-encased steel composite columns. *Journal of Structural Engineering, 130*, 1941–1953. https://doi.org/10.1061/(ASCE)0733-9445(2004)130:12(1941)

Mounica, I., Subramanian, S.A.V., Umamaheswari, N. (2022). Flexural behaviour of composite rectangular steel beams filled with concrete. (p. 020019).

Neville, A.M. (1995). Properties of concrete (vol. 4): Longman london.

Nguyen, P.-C., Tran, T.-T., Nguyen, H.-P., & Tran, T.-D. (2025). Nonlinear inelastic local buckling behavior of steel columns subjected to axial compression. *Civil Engineering Journal, 11*, 3916–3933. https://doi.org/10.28991/CEJ-2025-011-09-022

Ouyang, Y., & Kwan, A. K. (2018). Finite element analysis of square concrete-filled steel tube (cfst) columns under axial compressive load. *Engineering Structures, 156*, 443–459. https://doi.org/10.1016/j.engstruct.2017.11.055

Park, R. (1988). Ductility evaluation from laboratory and analytical testing. Proceedings of the 9th world conference on earthquake engineering (Vol. 8, p. 605–616). Tokyo-Kyoto Japan.

Parvin, A., & Brighton, D. (2014). Frp composites strengthening of concrete columns under various loading conditions. *Polymers, 6*, 1040–1056. https://doi.org/10.3390/polym6041040

Ren, Q. X., Zhou, K., Hou, C., Tao, Z., & Han, L. H. (2018). Dune sand concrete-filled steel tubular (cfst) stub columns under axial compression: Experiments. *Thin-Walled Structures, 124*, 291–302. https://doi.org/10.1016/j.tws.2017.12.006

Roeder, C. W., Lehman, D. E., & Thody, R. (2009). Composite action in cft components and connections. *Engineering Journal, 46*, 229–242. https://doi.org/10.62913/engj.v46i4.967

Sakino, K., Nakahara, H., Morino, S., & Nishiyama, I. (2004). Behavior of centrally loaded concrete-filled steel-tube short columns. *Journal of Structural Engineering, 130*, 180–188. https://doi.org/10.1061/(ASCE)0733-9445(2004)130:2(180)

Shanmugam, N. (2022). Concrete-filled steel box columns. In Analysis and design of plated structures (p. 403–436). Elsevier.

Shen, L., Ding, M., Feng, C., Alqawzai, S., Elchalakani, M., & Yang, B. (2022). Axial compressive behavior of thin-walled concrete-filled double-skin steel tubular stub columns with connecting strips. *Journal of Structural Engineering, 148*(2), 04021267. https://doi.org/10.1061/(ASCE)ST.1943-541X.0003234

Sonnenschein, R., Gajdosova, K., & Gramblicka, S. (2020). Comparison of composite, steel and reinforced concrete columns. *IOP Conference Series: Materials Science and Engineering, 960*, Article 032093. https://doi.org/10.1088/1757-899X/960/3/032093

Su, M., Cai, Y., Chen, X., & Young, B. (2020). Behaviour of concrete-filled cold-formed high strength steel circular stub columns. *Thin-Walled Structures, 157*, Article 107078. https://doi.org/10.1016/j.tws.2020.107078

Sulaiman, A., Mustapha, F. A., & Mohamed, R. N. (2021). Performance of square steel tubular stub columns in-filled with fly ash and silica fume self-compacting concrete under concentric loading. *IOP Conference Series: Materials Science and Engineering, 1144*, Article 012030. https://doi.org/10.1088/1757-899x/1144/1/012030

Tan, K. F., & Liu, L. B. (2012). Mechanical properties of high strength concrete filled steel tubular columns. *Advanced Materials Research, 472–475*, 1119–1125. https://doi.org/10.4028/www.scientific.net/AMR.472-475.1119

Tao, Z., Han, L. H., & Wang, D. Y. (2008). Strength and ductility of stiffened thin-walled hollow steel structural stub columns filled with concrete. *Thin-Walled Structures, 46*, 1113–1128. https://doi.org/10.1016/j.tws.2008.01.007

Tao, Z., Han, L.-H., & Wang, Z.-B. (2005). Experimental behaviour of stiffened concrete-filled thin-walled hollow steel structural (hss) stub columns. *Journal of Constructional Steel Research, 61*, 962–983. https://doi.org/10.1016/j.jcsr.2004.12.003

Tao, Z., Han, L.-H., & Zhao, X.-L. (2004). Behaviour of concrete-filled double skin (chs inner and chs outer) steel tubular stub columns and beam-columns. *Journal of Constructional Steel Research, 60*, 1129–1158. https://doi.org/10.1016/j.jcsr.2003.11.008

Tawfic, Y. R., Sayed, A. S. A., Eid, M. A., & el Hafez, L. A. (2021). Experimental investigation to evaluate the behavior of concrete-filled steel tubular columns under the effect of the distribution of the total steel area between the internal concrete core and the external steel tube. *International Journal of Engineering Research in Africa, 54*, 86–99. https://doi.org/10.4028/www.scientific.net/JERA.54.86

Thomas, J., & Sandeep, T. (2020). Capacity of short circular cfst columns with inner vertical plates welded intermittently. *Journal of Constructional Steel Research, 165*, Article 105840. https://doi.org/10.1016/j.jcsr.2019.105840

Wang, F., Young, B., & Gardner, L. (2019). Compressive testing and numerical modelling of concrete-filled double skin chs with austenitic stainless steel outer tubes. *Thin-Walled Structures, 141*, 345–359. https://doi.org/10.1016/j.tws.2019.04.003

Wang, X., Fan, F., & Lai, J. (2022). Strength behavior of circular concrete-filled steel tube stub columns under axial compression: A review. *Construction and Building Materials, 322*, Article 126144. https://doi.org/10.1016/j.conbuildmat.2021.126144

Wang, Y., Chen, J., & Geng, Y. (2015). Testing and analysis of axially loaded normal-strength recycled aggregate concrete filled steel tubular stub columns. *Engineering Structures, 86*, 192–212. https://doi.org/10.1016/j.engstruct.2015.01.007

Wen, Y., Hu, Z., Li, A., Li, Q., Li, X., & Xu, Y. (2021). Experimental study on cfrp-confined circularized concrete-filled square steel tube short columns. *Advances in Materials Science and Engineering, 2021*(1), 6620577. https://doi.org/10.1155/2021/6620577

Xu, L., Hu, H.-S., Zhang, L.-L., Su, L.-H., Lu, W.-M., Chen, R.-Y., & Syed, H. B. (2025). Concentric axial load test for square cfst columns strengthened with steel jackets. *Journal of Constructional Steel Research, 229*, Article 109481. https://doi.org/10.1016/j.jcsr.2025.109481

Yan, Y., Xu, L., Li, B., Chi, Y., Yu, M., Zhou, K., & Song, Y. (2019). Axial behavior of ultra-high performance concrete (uhpc) filled stocky steel tubes with square sections. *Journal of Constructional Steel Research, 158*, 417–428. https://doi.org/10.1016/j.jcsr.2019.03.018

Yang, Y. F., Cao, K., & Wang, T. Z. (2013). Experimental behavior of cfst stub columns after being exposed to freezing and thawing. *Cold Regions Science and Technology, 89*, 7–21. https://doi.org/10.1016/j.coldregions.2013.01.005

Yang, Y.-F., & Han, L.-H. (2006). Compressive and flexural behaviour of recycled aggregate concrete filled steel tubes (racfst) under short-term loadings. *Steel and Composite Structures, 6*, 257–284. https://doi.org/10.12989/scs.2006.6.3.257

Youssef, M. N., Feng, M. Q., & Mosallam, A. S. (2007). Stress-strain model for concrete confined by frp composites. *Composites Part B: Engineering, 38*, 614–628. https://doi.org/10.1016/j.compositesb.2006.07.020

Yu, C. Q., Tong, G. S., Tong, J. Z., Zhang, J. W., Li, X. G., & Xu, S. L. (2024). Experimental and numerical study on seismic performance of l-shaped multi-cellular cfst frames. *Journal of Constructional Steel Research, 213*, Article 108360. https://doi.org/10.1016/j.jcsr.2023.108360

Yu, Q., Tao, Z., & Wu, Y.-X. (2008). Experimental behaviour of high performance concrete-filled steel tubular columns. *Thin-Walled Structures, 46*, 362–370. https://doi.org/10.1016/j.tws.2007.10.001

Yun, X., & Gardner, L. (2017). Stress-strain curves for hot-rolled steels. *Journal of Constructional Steel Research, 133*, 36–46. https://doi.org/10.1016/j.jcsr.2017.01.024

Zhan, Y., Zhao, R., Ma, Z. J., Xu, T., & Song, R. (2016). Behavior of prestressed concrete-filled steel tube (cfst) beam. *Engineering Structures, 122*, 144–155. https://doi.org/10.1016/j.engstruct.2016.04.050

Zhao, P., Huang, Y., Lu, Y., Liang, H., & Zhu, T. (2022). Eccentric behaviour of square cfst columns strengthened using square steel tube and high-performance concrete jackets. *Engineering Structures, 253*, Article 113772. https://doi.org/10.1016/j.engstruct.2021.113772

Zhou, X., Zhou, Z., & Gan, D. (2020). Analysis and design of axially loaded square cfst columns with diagonal ribs. *Journal of Constructional Steel Research, 167*, Article 105848. https://doi.org/10.1016/J.JCSR.2019.105848

Zhou, Z., Gan, D., & Zhou, X. (2019). Improved composite effect of square concrete-filled steel tubes with diagonal binding ribs. *Journal of Structural Engineering, 145*(10), 04019112. https://doi.org/10.1061/(ASCE)ST.1943-541X.0002400

Zhu, A., Zhang, X., Zhu, H., Zhu, J., & Lu, Y. (2017). Experimental study of concrete filled cold-formed steel tubular stub columns. *Journal of Constructional Steel Research, 134*, 17–27. https://doi.org/10.1016/j.jcsr.2017.03.003

Zhu, J., Chen, J., Zhang, L., Zhang, Y., & Chan, T.-M. (2023). Numerical investigation and design recommendation for thin-walled octagonal concrete filled steel tubes. *Thin-Walled Structures, 188*, Article 110801. https://doi.org/10.1016/j.tws.2023.110801

Zhu, J.-Y., & Chan, T.-M. (2019). Experimental investigation on steel-tube-confined-concrete stub column with different cross-section shapes under uniaxial-compression. *Journal of Constructional Steel Research, 162*, Article 105729. https://doi.org/10.1016/j.jcsr.2019.105729